

Electronic Thesis and Dissertation Repository

9-19-2014 12:00 AM

Three-dimensional Photoacoustic Tomography System Design Analysis and Optimization

Philip Wong, *The University of Western Ontario*

Supervisor: Dr. Jeffrey J.L. Carson, *The University of Western Ontario*

A thesis submitted in partial fulfillment of the requirements for the Master of Science degree in
Medical Biophysics

© Philip Wong 2014

Follow this and additional works at: <https://ir.lib.uwo.ca/etd>



Part of the [Medical Biophysics Commons](#)

Recommended Citation

Wong, Philip, "Three-dimensional Photoacoustic Tomography System Design Analysis and Optimization" (2014). *Electronic Thesis and Dissertation Repository*. 2484.

<https://ir.lib.uwo.ca/etd/2484>

This Dissertation/Thesis is brought to you for free and open access by Scholarship@Western. It has been accepted for inclusion in Electronic Thesis and Dissertation Repository by an authorized administrator of Scholarship@Western. For more information, please contact wlsadmin@uwo.ca.

THREE-DIMENSIONAL PHOTOACOUSTIC TOMOGRAPHY SYSTEM DESIGN
ANALYSIS AND OPTIMIZATION

(Thesis format: Integrated Article)

by

Philip Wong

Graduate Program in Medical Biophysics

A thesis submitted in partial fulfillment
of the requirements for the degree of
Master of Science

The School of Graduate and Postdoctoral Studies
The University of Western Ontario
London, Ontario, Canada

© Philip Wong 2014

Abstract

Photoacoustic tomography (PAT) is an emerging imaging modality capable of mapping optical absorption in tissues. It is a hybrid technique that combines the high spatial resolution of ultrasound imaging with the high contrast of optical imaging, and has demonstrated much potential in biomedical applications. Conventional PAT systems employ raster scanning to capture a large number of projections, thus improving image reconstruction at the cost of temporal resolution. Arising from the desire for real-time 3D PA imaging, several groups have begun to design PAT systems with staring arrays, where image acquisition is only limited by the repetition rate of the laser. However, there has been little emphasis on staring array design analysis and optimization. We have developed objective figures of merit for PAT system performance and applied these metrics to improve system design. The results suggested that the developed approach could be used to objectively characterize and improve any PAT system design.

Keywords: Photoacoustic imaging, Photoacoustic tomography, 3D imaging, System analysis, Crosstalk matrix, System design, System optimization

Co-Authorship Statement

This section describes the contribution from various authors for the work completed in Chapters 2 and 3.

Chapter 2: P. Wong, I. Kosik, J. J. L. Carson. “Objective assessment of 3D photoacoustic tomography by the spatial crosstalk matrix,” Article in preparation for submission to Journal of Biomedical Optics.

Ivan Kosik designed and manufactured the transducers and maintained the overall system. Dr. Carson aided in project design, edited the manuscript, and provided general project supervision. I designed and conducted the experiment, analyzed and interpreted the results, and wrote the manuscript.

Chapter 3: P. Wong, A. Raess, I. Kosik, J. J. L. Carson. “Design optimizations for 3D photoacoustic tomography staring array systems,” Article in preparation for submission to Applied Optics.

Ivan Kosik designed and manufactured the transducers and maintained the overall system. Avery Raess helped conduct transducer performance characterization. Dr. Carson aided in project design, edited the manuscript, and provided general project supervision. I designed and conducted the experiment, analyzed and interpreted the results, and wrote the manuscript.

Acknowledgments

It is always sobering to reflect on how quickly life passes by and this is especially true as I look back to the past two years of my Master's degree. Throughout these two years, there have been many people who have poured themselves into my work and my life, a few of whom I want to specifically mention and thank.

To Dr. Carson, it was a pleasure to pursue my Master's degree under your supervision. The enthusiasm and support you have shown towards my project has helped cultivate a greater enjoyment in learning and research. I look forward to continue working under your supervision.

To the rest of the Dr. Carson lab, each of your unique expressions of friendliness and encouragement to me has made my time here all the more enjoyable and fun.

To my parents, I'm thankful for the trust, patience, and love you guys show to me. The virtues you have taught and exemplified towards me will always be something I will strive to grow in.

To my friends, the times of fun and food have always brought a sense of simplicity and rest in my life. Our conversations about God and truth and joy and love were always fresh reminders of the important things in this life. I'm thankful for all the ways you guys have sharpened and transformed my thinking and way of life.

To my fiancée, Andrea, the decision to pursue a Master's degree meant that our relationship would be long-d from the start. Although sometimes it's been rough, I am thankful for the unmerited love and support you continue to shower upon me. As we enter marriage, I thank God for the way He has brought us together and the ways in which He will continue to sustain us.

I would like to also acknowledge the financial support provided by UWO, the Translational Breast Cancer Research Unit, and the Ontario Graduate Scholarship.

Table of Contents

Abstract.....	ii
Co-Authorship Statement.....	iii
Acknowledgments.....	iv
List of Figures.....	ix
List of Abbreviations and Symbols.....	xiii
Preface.....	xvi
Chapter 1.....	1
1 Introduction.....	1
1.1 Background.....	2
1.1.1 Medical Ultrasound.....	2
1.1.2 Biomedical optical technologies.....	3
1.1.3 Challenges in optical imaging.....	5
1.2 Principles of photoacoustic imaging.....	6
1.2.1 Photoacoustic wave generation.....	6
1.2.2 Photoacoustic wave propagation and detection.....	8
1.2.3 Instrumentation configurations.....	9
1.3 Photoacoustic tomography.....	10
1.3.1 Detection geometries.....	10
1.3.2 Image reconstruction approaches.....	11
1.4 System analysis.....	12
1.4.1 Singular value spectrum.....	13
1.4.2 Crosstalk matrix.....	14
1.5 Motivation and Objectives.....	14

1.6	References.....	15
Chapter 2..... 20		
2	Objective assessment of 3D photoacoustic tomography by the spatial crosstalk matrix	20
2.1	Introduction.....	20
2.1.1	Background.....	20
2.1.2	PAT system design	21
2.1.3	Fourier crosstalk matrix	21
2.1.4	Objective and approach.....	21
2.2	Materials and Methods.....	22
2.2.1	PAT system.....	22
2.2.2	Spatial crosstalk matrix.....	25
2.2.3	Calibration scan	26
2.2.4	Figures-of-Merit.....	27
2.3	Results.....	29
2.3.1	System sensitivity and aliasing	29
2.3.2	Figures-of-merit	32
2.4	Discussion.....	35
2.4.1	System sensitivity and aliasing	35
2.4.2	Figures-of-merit	36
2.5	Conclusion	36
2.6	Acknowledgments.....	37
2.7	References.....	37
Chapter 3..... 41		
3	Design improvement of a staring, sparse transducer array for 3D photoacoustic tomography using the spatial crosstalk matrix.....	41

3.1	Introduction.....	41
3.1.1	Background.....	41
3.1.2	Crosstalk matrix.....	42
3.1.3	Objective and Approach.....	42
3.2	Materials and Methods.....	42
3.2.1	Simulations: 3D PAT system.....	42
3.2.2	Simulations: system design improvements.....	44
3.3	Results.....	45
3.3.1	System design parameters: spatial crosstalk elements.....	45
3.3.2	System design assessment: FoM.....	50
3.4	Discussion.....	54
3.4.1	System coverage.....	54
3.4.2	System design assessment.....	54
3.4.3	System design strategies and considerations.....	56
3.5	Conclusion.....	57
3.6	Acknowledgments.....	57
3.7	References.....	58
	Chapter 4.....	60
4	Discussion and future work.....	60
4.1	Summary of work.....	60
4.2	System calibration improvements.....	61
4.3	System design considerations.....	62
4.3.1	Detector technologies.....	62
4.3.2	Virtual detectors and reflectors.....	63
4.4	System analysis considerations.....	65

4.4.1	The crosstalk matrix.....	65
4.4.2	Other figures of merit.....	65
4.5	Applications	67
4.5.1	Functional imaging	67
4.6	Conclusions.....	67
4.7	References.....	68
	Curriculum Vitae	72

List of Figures

Figure 1-1 Types of sound-tissue interactions: (a) attenuation, (b) absorption, (c) reflection, (d) scattering, and (e) refraction. The shade of the black arrow corresponds to the amplitude of the sound wave, where white is zero amplitude. (a) The sound wave attenuates as it travels through the circular object. (b) The sound wave is absorbed by the surrounding tissue and converted to heat. (c) The sound wave is reflected at the surface of the object. (d) The sound wave is propagated in many random directions. (e) The sound wave bends as it crosses a boundary. 3

Figure 1-2 Photoacoustic waveform in the (a) time domain and (b) frequency domain. The PA waveform in the frequency domain is plotted for two PA sources of different size (1 mm and 2 mm). 9

Figure 2-1 Staring transducer array design for 3D PAT. (a) A 3D CAD rendering of the plastic shell used to hold the transducers. (b) A 3D representation of the transducer locations. Darker shaded area represents exterior of shell closest to reader. Lighter shaded area represents interior surface of the shell. (c) Photograph of a custom-built transducer (left) and front face of the transducer (right). The red scale bar represents 1 cm. (d) Example of a photoacoustic pressure signal from a photoacoustic point source (~70-100 μm) averaged over 5 triggers acquired with one transducer at 40 MHz sampling rate. The amplitude represents the counts on the digital converter and ranges from ± 2048 counts. (e) Photograph of actual 3D PAT system. 24

Figure 2-2 (a) System sensitivity maps of the z-plane 3.5 mm below center (left column), center plane (middle column), and z-plane 3.5 mm above center (right column) as a function of transducer count and sampling rate. Maps were normalized to peak system sensitivity per sampling rate. (b) System sensitivity maps showing last row of (a) (96 transducers) normalized to peak system sensitivity across sampling rates. (c) Aliasing maps for the center voxel as a function of transducer count and sampling rate. Planes correspond to those shown in (a). Maps were normalized to peak system sensitivity per

sampling rate and per transducer count and then scaled to 20% max for display purposes.
 (d) Same as (c) but for aliasing for a voxel near the edge of object space. 31

Figure 2-3 FoM for system performance (clockwise from top left: RMSE, PSNR, MAE, and 3D-MSSIM) plotted as a function of transducer count and sampling rate (legend shown in panel (a))..... 33

Figure 2-4 Metric maps for (a) RMSE, (b) MAE, and (c) 3D-MSSIM displayed as a function of transducer count and sampling rate in the z-plane 3.5 mm below center (left column), center plane (middle column), and z-plane 3.5 mm above center (right column).
 34

Figure 3-1 (a) Transducer response profile to a PA point source (~70-100 μm) averaged over 64000 triggers acquired with one transducer at 40 MHz sampling rate. The amplitude represents the counts on the digital converter and has been normalized to the max sensitivity. (b) Point cloud representations of the experimental transducer arrangement (top) and uniform sampling arrangement (bottom). Darker shaded area represents exterior of shell closest to reader. Lighter shaded area represents interior surface of the shell. (c) Same as (b) from a side-view. (d) Normalized sensitivity maps for the two arrangements and scaled to 30% max sensitivity for display purposes. Aliasing maps for the center voxel (e) and a voxel along the left edge (f) shown for the two arrangements (experimental transducer arrangement in the top row and uniform sampling arrangement in the bottom row). Each arrangement was independently normalized and scaled to 10% max for display purposes. The image planes are $2 \times 2 \text{ cm}^2$ and correspond to every other xy-plane of object space (left to right corresponds to bottom ($z = -2 \text{ cm}$) to top ($z = 2 \text{ cm}$) planes at 1 mm step size)..... 47

Figure 3-2 (a) Point cloud representations of transducer arrays as a function of array angular coverage (top to bottom corresponds to 0° to 60°). (b) Same as (a) but from a side view. (c) Normalized sensitivity maps (scaled to 30% max for display purposes) for each array coverage angle (top to bottom row corresponds to 0° to 60°). (d) Independently normalized aliasing maps (scaled to 10% max for display purposes) for the center voxel

and left edge voxel (e) for each array coverage angle. Image planes correspond with those in Fig. 3-1..... 48

Figure 3-3 (a) Point cloud representations of transducer array as a function of array radius (top to bottom corresponds to 37.5 mm to 87.5 mm). (b) Same as (a) but from the top view. (c) Normalized sensitivity maps (scaled to 30% max for display purposes) for each array radius (top to bottom corresponds to 37.5 mm to 87.5 mm, respectively). (d) Independently normalized aliasing maps (scaled to 10% max for display purposes) for the center voxel and left edge voxel (e) for each array radius. Image planes correspond with those in Fig. 3-1. 49

Figure 3-4 Metric maps for (a) RMSE, (b) PSNR, (c) MAE, and (d) 3D-SSIM displayed for both experimental transducer arrangement (top row) and uniform sampling arrangement (bottom row). (e)-(h) System performance figures of merit (RMSE, PSNR, MAE, and 3D-SSIM reading clockwise starting from top left panel) plotted as a function of cubic shells for the two arrangements (legend shown in panel (e)). 51

Figure 3-5 Metric maps for (a) RMSE, (b) PSNR, (c) MAE, and (d) 3D-SSIM displayed as a function of array angular coverage (top to bottom corresponds to 0° to 60°). (e)-(h) System performance figures of merit (RMSE, PSNR, MAE, and 3D-SSIM reading clockwise starting from top left panel) plotted as a function of cubic shells with varying array angular coverage (legend shown in panel (e)). 52

Figure 3-6 Metric maps for (a) RMSE, (b) PSNR, (c) MAE, and (d) 3D-SSIM displayed as a function of array radius (top to bottom corresponds to 37.5 mm to 87.5 mm). (e)-(h) System performance figures of merit (RMSE, PSNR, MAE, and 3D-SSIM reading clockwise starting from top left panel) plotted as a function of cubic shells with varying array radius (legend shown in panel (e))..... 53

Figure 4-1 Virtual detector concept for a (a) synthetic aperture set up [11,12], (b) focused transducer [13], and (c) ring transducer [14], where the focal point is treated as the virtual detector. The virtual detector is then raster scanned around the object. (d) Illustration of

backscatterers as virtual detectors [16]. Acoustic waves containing information of the object at different projections are reflected towards detector. 64

List of Abbreviations and Symbols

2D	Two dimensional
3D	Three dimensional
4D	Four dimensional
AR-PAM	Acoustic resolution photoacoustic microscopy
cm	Centimeter
CMUT	Capacitive micromachined ultrasonic transducers
CS	Compressed sensing
CT	Computed tomography
dB	Decibel
EM	Electromagnetic radiation
FoM	Figures-of-merit
GPU	Graphic processing unit
IQA	Image quality assessment
J	Joule
K	Kelvin
LCI	Low-coherence interferometry
m	Meter
MAE	Mean absolute error
MHz	Megahertz

mm	Millimeter
MRI	Magnetic resonance imaging
ms	Millisecond
MSSIM	Mean structural similarity index
ns	Nanosecond
OCT	Optical coherence tomography
OR-PAM	Optical resolution photoacoustic microscopy
PA	Photoacoustic
PAI	Photoacoustic imaging
PAM	Photoacoustic microscopy
PAT	Photoacoustic tomography
PVQ	Perceptual visual quality
PSNR	Peak signal-to-noise ratio
RMSE	Root mean square error
ROI	Region of interest
s	second
SNR	Signal-to-noise ratio
SSIM	Structural similarity index
SVD	Singular value decomposition
US	Ultrasound

VQA	Video quality assessment
σ	Standard deviation
μm	Micrometer
μs	Microsecond
π	Pi

Preface

The work completed throughout the duration of my MSc degree at Western University and Lawson Health Research Institute is summarized in the four chapters of this dissertation.

Chapter 1 introduces the basic principles of photoacoustic imaging (PAI). A general overview of ultrasound and optical imaging techniques is described and the strengths PAI brings to the table are presented. The chapter discusses the various approaches taken for PAI and concludes with the motivation for my research.

Chapters 2 and 3 are based on manuscripts in preparation for submission to peer-reviewed journals that were written over the course of my degree. The first publication focused on the development of a methodology to objectively characterize system performance. Figures of merit were derived from the spatial crosstalk matrix. The second publication aimed to implement the developed methodology to improve different system design parameters.

Chapter 4 provides a summary of the work and discusses potential areas of future study.

Chapter 1

1 Introduction

Conventional medical imaging modalities, such as magnetic resonance imaging (MRI) and x-ray computed tomography (CT), offer various capabilities for clinical applications. The past two decades have witnessed the emergence of a new biomedical imaging technology—photoacoustic imaging (PAI) – that holds great potential in complementing these already existing technologies. An overview of the development of PAI is presented in this chapter.

Based on the photoacoustic (PA) effect, PAI integrates the strengths from both optical imaging and ultrasound imaging. Thus, PAI can be considered either as an ultrasound-mediated optical imaging modality or an ultrasound imaging modality with optically-enhanced contrast. In order to provide a better foundation for understanding PAI, general reviews of the building blocks of PAI— medical ultrasound (US) and biomedical optics – are introduced in this chapter. The principles of PA wave generation and propagation are described in detail, leading to a summary of different instrumentation configurations as well as various image reconstruction approaches.

Photoacoustic imaging systems are inherently shift-variant and different methods have been previously developed to characterize system response. Several system characterization techniques are described in this chapter along with their respective limitations. The objective of this work was to develop an improved system characterization approach (Chapter 2) and to apply this approach to improve system design (Chapter 3). The design strategies developed hold potential in optimizing system performance for any PAT staring array system. Technical details briefly introduced in Chapters 2 and 3 are described in greater detail in this chapter.

1.1 Background

Section 1.1.1 outlines the basic principles of US. A broad overview of optical imaging technologies that have moved from ‘bench-top to bedside’ is covered in section 1.1.2, highlighting the valuable complement that PAI can provide. Material in section 1.1.2 is adapted from Ref. [1].

1.1.1 Medical Ultrasound

Medical US imaging is a branch of sonar, extending object detection techniques that utilize sound propagation for medical diagnostics. Sound waves, similar to light waves, can interact with tissues in the following ways: reflection, scattering, refraction, absorption, and attenuation. (Fig. 1-1) [2].

Sound wave reflection occurs at the interfaces between objects with different acoustic impedances. The acoustic impedance of an object can be expressed as:

$$Z = \rho c \quad (1.1)$$

where ρ is density and c is the speed of sound in the medium. The degree of reflection is proportional to the impedance mismatch between objects. For example, the interface between soft tissue and bone would generate a large reflection. **Scattering refers to the process where sound is propagated in many directions.** This can act to enhance the visualization of medical US. Refraction occurs when sound waves are redirected at an oblique angle relative to the direction of the sound wave, usually occurring at smooth interfaces with high acoustic impedance. This is due to the change in speed of the sound wave as it crosses from one material to another. When a sound wave travels through tissue, its energy is distributed spatially and converted to heat. Absorption refers to the uptake of the sound wave energy by the surrounding medium and attenuation refers to the decrease in energy of the original sound wave. The propagation time of sound can be accurately measured and by applying the principles of echo localization, differences in acoustic impedance between tissues are mapped into an image.

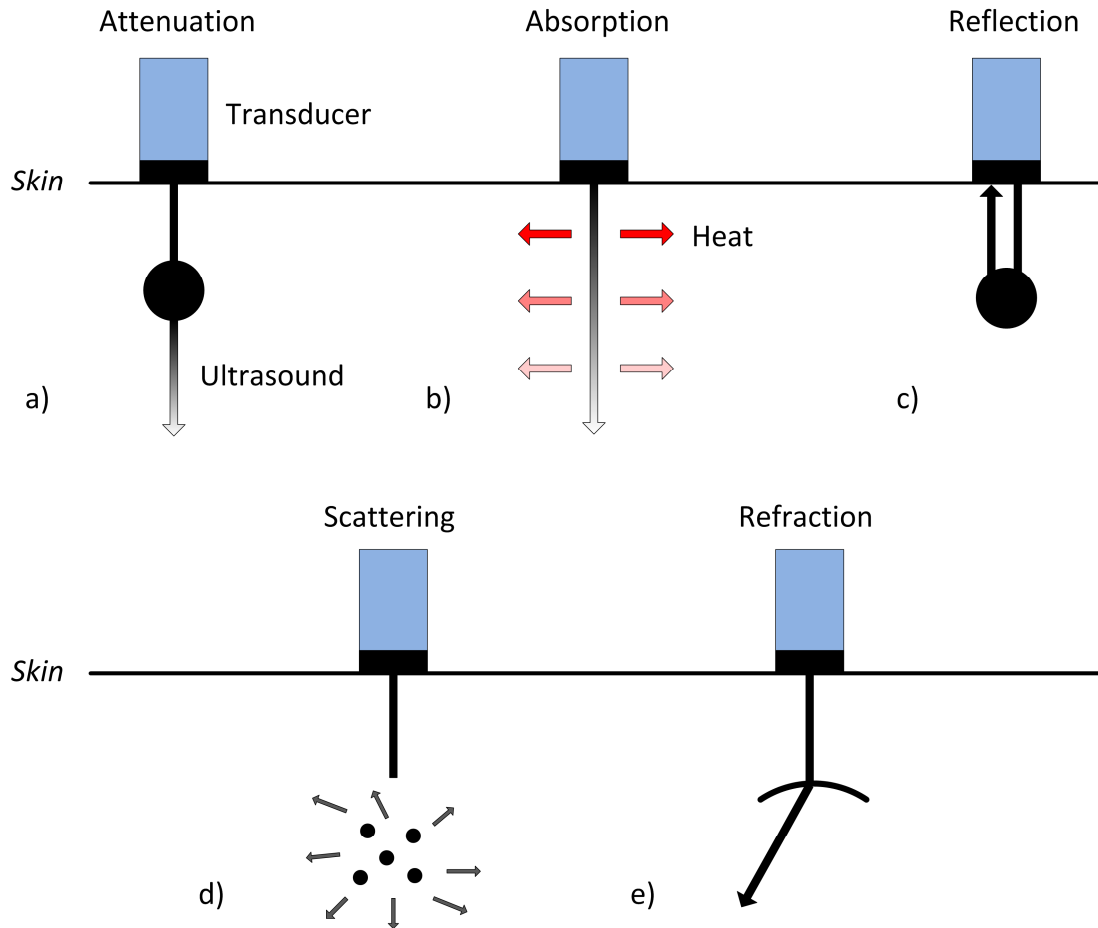


Figure 1-1 Types of sound-tissue interactions: (a) attenuation, (b) absorption, (c) reflection, (d) scattering, and (e) refraction. The shade of the black arrow corresponds to the amplitude of the sound wave, where white is zero amplitude. (a) The sound wave attenuates as it travels through the circular object. (b) The sound wave is absorbed by the surrounding tissue and converted to heat. (c) The sound wave is reflected at the surface of the object. (d) The sound wave is propagated in many random directions. (e) The sound wave bends as it crosses a boundary.

1.1.2 Biomedical optical technologies

The field of biomedical optics is a rapidly emerging area of research and covers a wide range of imaging techniques. By exploiting different light-tissue interactions, optical imaging has demonstrated a wide array of biomedical applications ranging from clinical diagnosis to molecular biology. Specifically in the clinical setting, some of the advantages that enable optimal imaging techniques to have considerable impact on disease treatment and prevention are the following: (i) capable of visualizing functional and structural changes with high spatial resolution and sensitivity; (ii) non-invasive and

non-ionizing; (iii) portable and cost efficient; (iv) capable of real-time imaging; (v) scalable (i.e. can be adapted to provide information in both microscopic and macroscopic scales); and (vi) enable quantitative analysis of data. Recent optical imaging techniques that have been applied clinically include, but are not limited to, spectral imaging, optical coherence tomography, confocal imaging, and molecular imaging.

Spectroscopy exploits the wavelength-dependent optical properties exhibited by many biomolecules in cells and tissues. Depending on the intended optical property to be measured, different spectroscopic techniques have been developed to measure light-tissue interaction as a function of wavelength. For instance, some possible light-tissue interactions are absorption, elastic scattering, fluorescence, and inelastic scattering. The corresponding spectroscopic techniques are absorption spectroscopy, diffuse reflectance spectroscopy, fluorescence spectroscopy, and Raman spectroscopy, respectively.

Spectroscopy enables high spectral resolution, but has poor spatial resolution. Due to high tissue spatial heterogeneity, spectroscopic applications in diagnostic capabilities are seriously limited. Furthermore, differences in spectra between normal and diseased tissues are subtle. In order to address this problem, imaging systems have been integrated with spectroscopy resulting in what is known as spectral imaging. Spectral imaging allows for both high spatial and spectral resolution in a single modality. A datacube is generated by capturing 2D images at different wavelengths and insight into the properties of the sample are extracted after data processing.

Optical coherence tomography (OCT) is a non-invasive, non-contact imaging modality capable of imaging sub-surface tissue structure with sub-micrometer resolution. For comparison, MRI, CT, and US only offer millimeter to sub-millimeter resolution. The basic system components of OCT include an interferometer (typically a Michelson interferometer), a broad-band, low-coherence light source, light splitting optics, fiber optics and an optical sensor. By emitting a temporally gated optical pulse, scattering events within the sample are localized using low-coherence interferometry (LCI) and mapped into an image. Thus, the principle of operation of OCT can be considered as the optical analogue of US. It is important to note that light travels approximately a million times faster than sound and current electronic detection systems are unable to accurately

measure echo time delays. Hence, correlation techniques are normally used to indirectly measure these delays. Although OCT is capable of capturing extremely high resolution images, it is limited to depths of 1-2 mm.

A confocal imaging system is a special type of scanning optical microscope. It improves the contrast of microscope images by positioning a pinhole in front of the photodetector, allowing only light that passes through the pinhole to be detected. In essence, the photodetector combined with the pinhole acts as a point detector. The object to be imaged is usually stained with a fluorescent dye and is illuminated with a small, focused laser beam. Light outside the focal plane is rejected by the pinhole and the reflected, transmitted, or fluorescent light is detected and stored. The image of the object is generated by raster scanning the laser beam across the object. The beam can also be focused at different depths for 3D imaging.

Imaging events *in vivo* at the molecular or genetic level is known as molecular imaging. Molecular imaging seeks to non-invasively visualize normal and abnormal cellular processes in real-time. With the assistance of optical biomarkers, specific molecules can be selected to emit amplified optical signals. This approach finds its chief clinical application in optically biomarking specific cancer molecular signatures. The pharmacokinetics of biomarkers *in vivo* is another strong characterization parameter for normal and abnormal cells. Due to the high proliferation rate of high-grade cancer cells, there are clear functional changes that differentiate it from a healthy cell. Dynamic spectral imaging is able to measure these changes.

1.1.3 Challenges in optical imaging

High-resolution optical imaging faces two principal challenges: diffraction and diffusion [3]. The spatial resolution is determined by the diffraction limit, whereas penetration depth is determined by diffusion. Recently, the resolution of optical imaging has been improved beyond the diffraction limit [4–7] and for the purpose of this work, only penetration depth is addressed.

Biological tissues strongly scatter light. Since most mainstream optical technologies rely on either optical scattering or fluorescent contrast, it is difficult to image past a few centimeters in biological tissues. Photoacoustic imaging has provided a unique way to resolve deep imaging of biological tissues by relying on tissue optical absorption [8].

1.2 Principles of photoacoustic imaging

Photoacoustic imaging relies on the optical absorption properties of biological tissues. Tissue is pulsed with laser light and the deposited optical energy is rapidly converted into heat. The slight increase in temperature (on the order of millikelvins) leads to an initial pressure increase followed by a subsequent relaxation, thereby emitting a broadband acoustic wave into its surroundings. Photoacoustic images are formed by detecting and localizing the position of these acoustic wave sources (Fig. 1-2(b)). **When a tissue sample is imaged ex vivo, it is placed into a coupling medium, typically water.** The theory of PA wave generation and propagation is described in greater detail in sections 1.2.1 and 1.2.2 and the material is adapted from Ref. [9] and Ref. [10]

1.2.1 Photoacoustic wave generation

Several techniques have been discovered to generate PA waves, but for medical imaging, we are mainly interested in PA waves generated from pulsed electromagnetic (EM) radiation. Aforementioned above, the generation of PA waves is based on the PA effect. This refers to the generation of sound waves arising from a thermoelastic expansion induced by a small increase in temperature when an object absorbs incident EM energy. The EM absorption and the scattering, thermal, and elastic properties of the sample determine the location of the excited PA signal.

There are two conditions that must be met in order for the PA effect to occur efficiently. The first condition is referred to as thermal confinement, which characterizes thermal diffusion. The time scale in which heat dissipation of absorbed EM radiation must occur (i.e. thermal relaxation time) can be expressed by:

$$\tau_{th} = L_p^2 / 4D_T \quad (1.2)$$

where L_p is the characteristic linear dimension of the tissue volume being heated and D_T is the thermal diffusivity (cm^2/s) of the sample. The L_p is dependent on the penetration depth of the EM wave or the size of the absorbing structure. Soft tissues typically have a D_T of approximately $1.4 \times 10^{-3} \text{ cm}^2/\text{s}$. The geometry of the heated volume is another factor that influences the estimation of τ_{th} . Thermal confinement is achieved when the excitation pulse width, τ_p , is shorter than τ_{th} , signifying that heat dissipation is negligible during the excitation pulse. This condition is typically met (see below for an example calculation).

The second condition for efficient generation of PA waves is referred to as stress confinement, which characterizes the pressure propagation. The stress relaxation time can be expressed as:

$$\tau_s = L_p/c \quad (1.3)$$

where c is the speed of sound in the respective medium. The speed of sound in soft tissues is $\sim 1500 \text{ m/s}$. Similarly, stress confinement is achieved when τ_p is shorter than τ_s . This allows for rapid increase of high thermoelastic pressure in the sample. From the thermal and stress relaxation time equations, it can be observed that the stress confinement condition is more stringent. For instance, to achieve a spatial resolution at $L_p = 150 \text{ }\mu\text{m}$, $\tau_{th} \sim 40 \text{ ms}$ and $\tau_s \sim 100 \text{ ns}$.

Provided that both thermal and stress confinement conditions are satisfied, thermal expansion causes a local pressure change that can be estimated by:

$$p_0 = (\beta c^2/C_p)\mu_a F = \Gamma A \quad (1.4)$$

where β is the isobaric volume expansion coefficient in K^{-1} , C_p is the specific heat in $\text{J}/(\text{K kg})$, μ_a is the absorption coefficient in cm^{-1} , F is the local light fluence in J/cm^2 , A is the local energy deposition density in J/cm^3 ($A = \mu_a F$), and Γ is referred to as the Grüneisen coefficient expressed as $\Gamma = \beta c^2/C_p$. A typical μ_a value for soft tissue is $\sim 0.1 \text{ cm}^{-1}$ and $\sim 1.6 \text{ cm}^{-1}$ for blood. The Grüneisen parameter relates pressure increase to the deposited EM energy and is considered relatively constant.

1.2.2 Photoacoustic wave propagation and detection

The general equation describing the propagation of the photoacoustic pressure wave is given by:

$$\left(\nabla^2 - \frac{1}{c_s^2} \frac{\partial^2}{\partial t^2}\right) p(\mathbf{r}, t) = -\frac{\beta}{\kappa c_s^2} \frac{\partial^2 T(\mathbf{r}, t)}{\partial t^2} \quad (1.5)$$

where $p(\mathbf{r}, t)$ denotes the acoustic pressure at location \mathbf{r} and time t and T is the excess temperature induced by EM absorption. The left-hand term describes the wave propagation and the right-hand term represents the source term. A detailed treatment of the derivation of the acoustic wave equation is given in Ref. [10]. The PA waves outgoing from an acoustic source can be detected by an US transducer at the object surface. Several characteristic features of the PA source can be derived from the shape of the signal. Here, the derivation from a PA monopole source of radius R_s is used as an instructive tool.

Assuming uniform optical absorption and illumination, the pressure profile of a PA monopole source results in a bipolar wave, also known as an N-shaped wave (Fig. 1-2(a)). The positive magnitude represents a diverging spherical pressure wave from the PA source (compression), whereas the negative magnitude represents a converging spherical pressure wave (rarefaction). There are three main features that can be derived from this bipolar wave. Firstly, the arrival time of the PA wave indicates the distance of the object from the transducer. Secondly, the time difference between the positive and negative peaks provides insight to the size of the source. Lastly, the amplitude of the signal is proportional to the optical absorption of the PA source and laser fluence (Eq. 1.4). Due to the abrupt edges of the bipolar wave, the PA signal contains a broad band of harmonics (Fig. 1-2(b)). As the size of the PA source decreases, the maximum value of the ultrasonic frequency increases. Therefore, broadband transducers are valuable in PAI to accurately measure objects of decreasing dimension. It is important to note that the emission efficiency of the transducer does not factor into the detection process. Thus, transducers used for PAI can be specifically designed with high receiving sensitivity. These transducers are typically made from piezoelectric material, having desirable

properties such as low thermal noise, high sensitivity, and broad bandwidth. The sensitivity of piezoelectric transducers, however, scales with size, making miniaturization a key challenge for photoacoustic imaging.

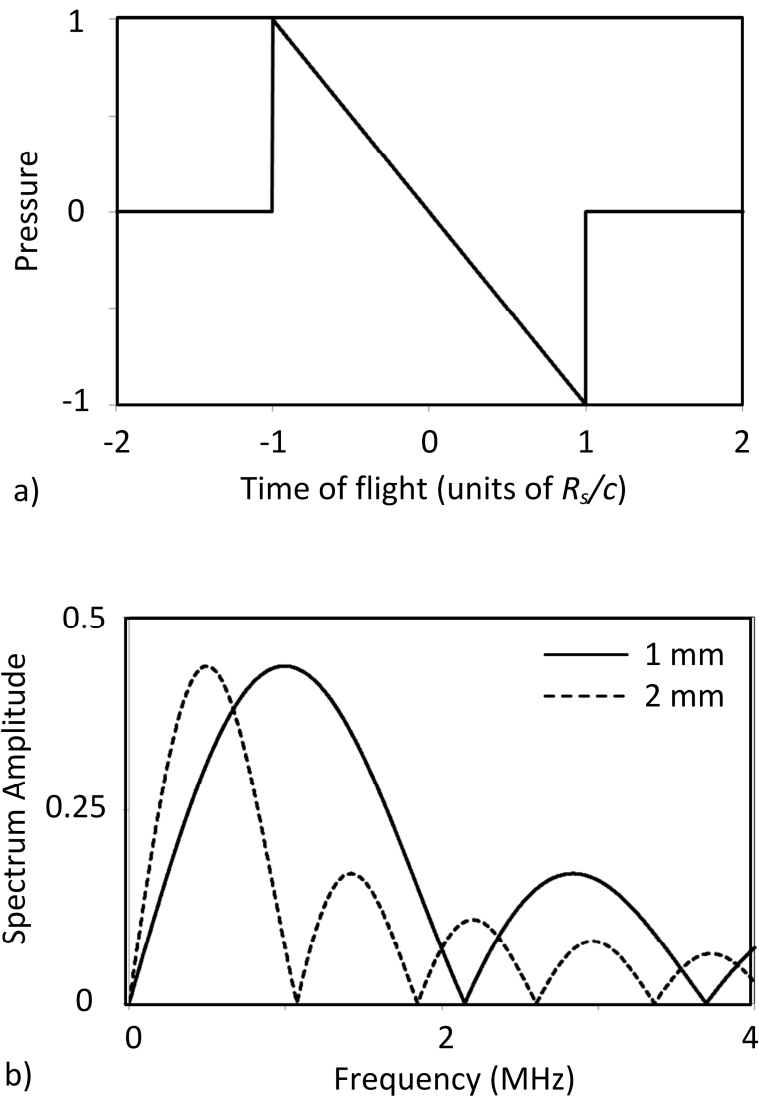


Figure 1-2 Photoacoustic waveform in the (a) time domain and (b) frequency domain. The PA waveform in the frequency domain is plotted for two PA sources of different size (1 mm and 2 mm).

1.2.3 Instrumentation configurations

Photoacoustic imaging systems can be classified into two main categories according to their imaging formation mechanisms: PA microscopy (PAM) and PA tomography (PAT)

[11]. Photoacoustic microscopy utilizes either a focused US detector or focused laser beam to construct an image from a set of acquired A-lines. When a focused US detector is used, the axial and lateral spatial resolution is determined by the properties of the transducer (i.e. central frequency and bandwidth). This approach is termed acoustic resolution PAM (AR-PAM). On the other hand, when a focused laser beam is used, the spatial resolution (in at least one plane) is defined by the spatial characteristics of the laser beam. This approach is termed optical resolution PAM (OR-PAM). The work presented in this dissertation is primarily concerned with PAT and a more detailed description of PAT is given in section 1.3.

1.3 Photoacoustic tomography

1.3.1 Detection geometries

Photoacoustic tomography can be regarded as the classical and most flexible PAI approach in terms of practical implementation. The PAT system incorporates a mechanically scanned ultrasound receiver or a staring array of receivers, which collects PA signals emitted from an irradiated sample. After the signals are recorded, a reconstruction algorithm is employed to generate an image. Both PAT synthetic apertures and staring arrays implement the same reconstruction algorithm. The latter, however, allows for high temporal resolution by bypassing mechanical scanning.

An object is considered to be in full view when each point of the object can be detected by the sensor surface with 4π steradians, that is, PA signals are collected from all directions. A closed spherical surface or a cylindrical surface of infinite length meets this level of coverage. Imaging in full view, however, is difficult in practical applications and often not feasible. For example, breast imaging limits the solid angle of detection to at most 2π steradians (hemisphere). When full view is not achieved, the data collected is incomplete and the unmeasured data is typically zeroed or estimated from the measured data. Some high-frequency information is lost in limited-view imaging, usually resulting in artifacts at the edges of the object.

Three common array geometries for PAT are spherical, cylindrical, and planar detection geometries [11]. A spherical scanner allows for the full enclosure of a region of interest (ROI) and thus, provides high image quality (large angular aperture). Cylindrical scanners are widely utilized due to their ease of use and also retain high image quality. Similar to spherical scanners, cylindrical scanners are commonly implemented for small-animal and breast imaging. The versatility of planar scanners makes it capable of imaging highly superficial features, such as the skin, whereas spherical and cylindrical scanners are poorly designed for this task. Image quality in planar scanners, however, is compromised due to poor coverage of the imaging volume. Photoacoustic tomography has been successful in visualizing many various objects. Examples include whole-body small animal vasculature [12], breast tumours [13,14], flow dynamics [15], small animal brains [16,17], and human vasculature [18].

1.3.2 Image reconstruction approaches

Photoacoustic image reconstruction is an inverse problem, where PA sources are mapped into image-space from measured pressure signals. The classic approach for PAT image reconstruction is back-projection. Typically, a single ultrasound transducer is mechanically scanned around the sample, thereby acquiring PA waves from many angles. The back-projection algorithm [19] is then implemented to reconstruct an image. There are a wide variety of other image reconstruction algorithms that have been developed for PAT. For instance, approximations have been applied to the standard Radon transform to tailor it for PAT reconstruction [20,21]. Delay-and-sum and synthetic aperture algorithms for US imaging have been successfully applied to PAT reconstruction [22,23]. Recently, analytical algorithms in the Fourier-domain and time-domain have also been derived for PAT reconstruction [24–26].

With the increasing importance of visualizing dynamic processes in 3D, Ephrat et al. developed a 3D real-time technique capable of acquiring PA images at the firing rate of the laser [27]. This was done by treating the image reconstruction problem as a linear model:

$$g = Hf + e \quad (1.6)$$

where g represents the measured data set, H is the imaging operator (also described elsewhere as the system matrix or forward model), f represents the unknown object(s), and e represents a noise process. The aim is to estimate f from the noisy data g but in most real situations the problem is ill-posed. A linear regularization procedure is usually applied in order to minimize estimation error. Ephrat et al. implemented a model-based inversion technique based on calculating the Moore-Penrose pseudoinverse with singular value decomposition (SVD) [28]. The imaging operator, H , can be decomposed by SVD as

$$H = USV^T \quad (1.7)$$

where U and V^T are unitary matrices and S is a diagonal matrix with non-zero diagonal entries consisting of the singular values of the imaging operator in decreasing order. The pseudoinverse of H is given by

$$H^\dagger = VS^\dagger U^T \quad (1.8)$$

where S^\dagger is computed by taking the reciprocal of each non-zero element above a given threshold on the diagonal of S . The level of regularization is controlled by thresholding lower singular values. As singular values in S decrease, the contribution from corresponding singular vectors also decreases. The unknown object(s), f , is then estimated by

$$f = H^\dagger g \quad (1.9)$$

This approach reduces the image reconstruction problem to a simple and fast matrix multiplication. Additionally, it has recently been shown that this image reconstruction technique outperformed traditional PA image reconstruction techniques under simulated clinical conditions [29].

1.4 System analysis

System performance can often be evaluated using a task-related figure-of-merit but when there are multiple tasks in mind, designers often seek generic figures-of-merit (FoM). Image reconstruction techniques have their own advantages and disadvantages beyond what is dictated by inherent system properties. Generic FoM that are independent of

imaging task or the specific selection of image reconstruction algorithm used may provide better insight into system performance. One approach to derive generic FoM for 3D PAT system performance is to consider the continuous-to-discrete sampling qualities of the system. The continuous object to be imaged can be represented by a linear combination of basis functions, mapping the object into a discrete representation with a certain resolution. Thus, system performance is related to how well the basis function coefficients are recovered. A common technique to assess this relation is the SVD. We previously introduced a higher level FoM based on the SVD to the field of 3D PAT system characterization [28].

1.4.1 Singular value spectrum

The metric derived from the SVD was based on examining the singular value spectrum. The number of effective singular values (i.e. effective rank of the imaging operator) was proportional to the number of coefficients (voxels) recoverable. The effective rank of the operator can be mathematically represented by:

$$\alpha_t \gg \alpha_{t+1} \quad (1.10)$$

where α represents the magnitude of the singular value and t is the effective rank of the matrix. The threshold can be estimated more precisely by:

$$\alpha_t/\alpha_{t+1} = \max\left(\alpha_j/\alpha_{j+1}\right), j = 1, 2, \dots, M \quad (1.11)$$

It is important to recognize that the singular values decrease as the columns of V^T contribute less useful information to the object space.

However, this FoM was difficult to interpret for comparison between two imaging system setups. The comparison would be ambiguous due to each imaging system having its own SVD and consequently, represented by its own unique set of singular vectors. Recovering N components from one system could produce a drastically different image in the other system for the same number of N components. Moreover, the SVD is a computationally expensive problem and would be inefficient for optimizing tasks with larger system matrices, characteristic of 3D problems.

1.4.2 Crosstalk matrix

First introduced by Barrett and Gifford, the Fourier crosstalk matrix is a formulation shown to be an effective assessment technique for system design [30]. The Fourier crosstalk matrix provides insight into the contribution from each Fourier coefficient to the data as well as the amount of overlap between coefficients. Specifically, the diagonal elements of the matrix describe the strength of every Fourier coefficient in the data, being analogous to the generalized transfer function, while the off-diagonal elements represent the degree of linear dependency between any two Fourier coefficients [30]. The Fourier crosstalk matrix can be related to the Fisher information matrix, and hence, to task performance [31]. It has been successfully applied to characterize system design of cone-beam tomography [30], hybrid positron emission tomography (PET) [32], and computed tomography imaging spectrometry (CTIS) [33].

A more detailed description of analyzing imaging systems using the crosstalk matrix is given in sections 2.2.2. The crosstalk concept can be generalized to any basis functions that are appropriate for representing objects in image space. Photoacoustic tomography is inherently a shift-variant imaging system and voxel (or pixel) basis functions are usually implemented instead of Fourier basis functions [27,34].

1.5 Motivation and Objectives

Accurate reconstruction of PA images requires detection of photoacoustic signals from many angles and broader signal bandwidth than can be provided by conventional linear ultrasound arrays. In order to increase the number of projections, a wide variety of PAT systems have been built implementing a raster scanning approach. Raster scanning, however, is difficult to extend to the 3D regime without compromising temporal resolution. In pursuit of fast 3D real-time imaging, several groups have begun to adopt PA systems with staring arrays, but assessment of array performance has been limited. We previously reported on a technique to calibrate a 3D PAT staring array system and

implemented different system characterization techniques. Nevertheless, these characterization metrics were impractical for system design optimization procedures.

The focus of Chapter 2 was aimed towards developing an improved system characterization technique. Our earlier work [35] used the experimentally constructed spatial (or voxel) crosstalk matrix for a 15-element 3D PAT system. We observed that the spatial crosstalk matrix qualitatively reflected changes in system performance as the transducer count and sampling rate were varied. Based on these qualitative findings, we were motivated to investigate quantitative FoM derived from the spatial crosstalk matrix to quantitatively compare performance across different 3D PAT system designs.

The image reconstruction approach developed by Ephrat et al. improved the temporal resolution of our 3D PAT system to be able to capture a single 3D PAT image per laser pulse. There has been little emphasis, however, on optimizing the spatial acoustic coverage of PAT staring array systems. The work in Chapter 3 utilized the FoM as a basis for improving our 3D PAT system design (according to spatial acoustic coverage) and three PAT staring array design parameters were examined: transducer arrangement, array angular coverage, and array radius.

1.6 References

- [1] C. Balas, “Review of biomedical optical imaging—a powerful, non-invasive, non-ionizing technology for improving in vivo diagnosis,” *Meas. Sci. Technol.* **20**(10), 104020 (2009) [doi:10.1088/0957-0233/20/10/104020].
- [2] G. Schmidt and B. Beuscher-Willems, *Ultrasound*, Georg Thieme Verlag, New York (2007).
- [3] L. V Wang, “Multiscale photoacoustic microscopy and computed tomography.,” *Nat. Photonics* **3**(9), 503–509, Nature Publishing Group (2009) [doi:10.1038/nphoton.2009.157].

- [4] A. Jost and R. Heintzmann, “Superresolution Multidimensional Imaging with Structured Illumination Microscopy,” *Annu. Rev. Mater. Res.* **43**(1), 261–282 (2013) [doi:10.1146/annurev-matsci-071312-121648].
- [5] G. Patterson, M. Davidson, S. Manley, and J. Lippincott-Schwartz, “Superresolution imaging using single-molecule localization.,” *Annu. Rev. Phys. Chem.* **61**, 345–367 (2010) [doi:10.1146/annurev.physchem.012809.103444].
- [6] S. W. Hell, “Far-Field Optical Nanoscopy,” 1153–1158 (2007).
- [7] E. Betzig, G. H. Patterson, R. Sougrat, O. W. Lindwasser, J. S. Bonifacino, M. W. Davidson, J. Lippincott-schwartz, F. Hess, W. Lindwasser, et al., “Imaging Proteins Intracellular at Nanometer Fluorescent Resolution,” 1642–1645 (2006).
- [8] S. Hu, K. Maslov, and L. V Wang, “Biomedical Optical Imaging Technologies,” R. Liang, Ed., Springer Berlin Heidelberg, Berlin, Heidelberg (2013) [doi:10.1007/978-3-642-28391-8].
- [9] M. Xu and L. V. Wang, “Photoacoustic imaging in biomedicine,” *Rev. Sci. Instrum.* **77**(4), 041101 (2006) [doi:10.1063/1.2195024].
- [10] L. V. Wang and H.-I. Wu, *Biomedical optics: principles and imaging*, John Wiley & Sons, Hoboken, New Jersey (2007).
- [11] P. Beard, “Biomedical photoacoustic imaging.,” *Interface Focus* **1**(4), 602–631 (2011) [doi:10.1098/rsfs.2011.0028].
- [12] H.-P. Brecht, R. Su, M. Fronheiser, S. a Ermilov, A. Conjusteau, and A. a Oraevsky, “Whole-body three-dimensional optoacoustic tomography system for small animals.,” *J. Biomed. Opt.* **14**(6), 064007 (2009) [doi:10.1117/1.3259361].
- [13] R. a. Kruger, R. B. Lam, D. R. Reinecke, S. P. Del Rio, and R. P. Doyle, “Photoacoustic angiography of the breast,” *Med. Phys.* **37**(11), 6096 (2010) [doi:10.1118/1.3497677].

- [14] S. a Ermilov, T. Khamapirad, A. Conjusteau, M. H. Leonard, R. Lacewell, K. Mehta, T. Miller, and A. a Oraevsky, “Laser optoacoustic imaging system for detection of breast cancer.,” *J. Biomed. Opt.* **14**(2), 024007 (2012)
[doi:10.1117/1.3086616].
- [15] H. Fang, K. Maslov, and L. V. Wang, “Photoacoustic Doppler flow measurement in optically scattering media,” *Appl. Phys. Lett.* **91**(26), 264103 (2007)
[doi:10.1063/1.2825569].
- [16] W. Lu, Q. Huang, G. Ku, X. Wen, M. Zhou, D. Guzatov, R. Su, A. Oraevsky, L. V Wang, et al., “Photoacoustic imaging of living mouse brain vasculature using hollow gold nanospheres,” *Biomaterials* **31**(9), 1–21 (2011)
[doi:10.1016/j.biomaterials.2009.12.007.Photoacoustic].
- [17] X. Wang, G. Ku, M. a Wegiel, D. J. Bornhop, G. Stoica, and L. V Wang, “Noninvasive photoacoustic angiography of animal brains in vivo with near-infrared light and an optical contrast agent.,” *Opt. Lett.* **29**(7), 730–732 (2004).
- [18] M. P. Fronheiser, S. a Ermilov, H.-P. Brecht, A. Conjusteau, R. Su, K. Mehta, and A. a Oraevsky, “Real-time optoacoustic monitoring and three-dimensional mapping of a human arm vasculature.,” *J. Biomed. Opt.* **15**(2), 021305 (2010)
[doi:10.1117/1.3370336].
- [19] M. Xu and L. Wang, “Universal back-projection algorithm for photoacoustic computed tomography,” *Phys. Rev. E* **71**(1), 016706 (2005)
[doi:10.1103/PhysRevE.71.016706].
- [20] Y. Xu, L. V. Wang, G. Ambartsoumian, and P. Kuchment, “Reconstructions in limited-view thermoacoustic tomography,” *Med. Phys.* **31**(4), 724 (2004)
[doi:10.1118/1.1644531].
- [21] V. G. Andreev, D. a. Popov, D. V. Sushko, A. a. Karabutov, and A. a. Oraevsky, “Image Reconstruction in 3D Optoacoustic Tomography System

with Hemispherical Transducer Array,” 10 June 2002, 137–145
[doi:10.1117/12.469858].

- [22] C. Hoelen and F. de Mul, “Image reconstruction for photoacoustic scanning of tissue structures,” *Appl. Opt.* (2000).
- [23] K. Köstli, M. Frenz, and H. Weber, “Optoacoustic tomography: time-gated measurement of pressure distributions and image reconstruction,” *Appl. ...* (2001).
- [24] Y. Xu, D. Feng, and L. V Wang, “Exact frequency-domain reconstruction for thermoacoustic tomography--I: Planar geometry.,” *IEEE Trans. Med. Imaging* **21**(7), 823–828 (2002).
- [25] M. Xu and L. V Wang, “Time-domain reconstruction for thermoacoustic tomography in a spherical geometry.,” *IEEE Trans. Med. Imaging* **21**(7), 814–822 (2002) [doi:10.1109/TMI.2002.801176].
- [26] D. Finch and S. K. Patch, “Determining a Function from Its Mean Values Over a Family of Spheres,” *SIAM J. Math. Anal.* **35**(5), 1213–1240 (2004)
[doi:10.1137/S0036141002417814].
- [27] P. Ephrat, M. Roumeliotis, F. S. Prato, and J. J. L. Carson, “Four-dimensional photoacoustic imaging of moving targets.,” *Opt. Express* **16**(26), 21570–21581 (2008).
- [28] M. B. Roumeliotis, R. Z. Stodilka, M. a Anastasio, E. Ng, and J. J. L. Carson, “Singular value decomposition analysis of a photoacoustic imaging system and 3D imaging at 0.7 FPS.,” *Opt. Express* **19**(14), 13405–13417 (2011).
- [29] A. Petschke and P. J. La Rivière, “Comparison of photoacoustic image reconstruction algorithms using the channelized Hotelling observer.,” *J. Biomed. Opt.* **18**(2), 26009 (2013) [doi:10.1117/1.JBO.18.2.026009].
- [30] H. H. Barrett and H. Gifford, “Cone-beam tomography with discrete data sets.,” *Phys. Med. Biol.* **39**(3), 451–476 (1994).

- [31] H. H. Barrett, J. L. Denny, R. F. Wagner, and K. J. Myers, "Objective assessment of image quality. II. Fisher information, Fourier crosstalk, and figures of merit for task performance.," *J. Opt. Soc. Am. A. Opt. Image Sci. Vis.* **12**(5), 834–852 (1995).
- [32] R. Z. Stodilka, E. J. Soares, and S. J. Glick, "Characterization of tomographic sampling in hybrid PET using the Fourier crosstalk matrix.," *IEEE Trans. Med. Imaging* **21**(12), 1468–1478 (2002) [doi:10.1109/TMI.2002.806595].
- [33] J. F. Scholl, "The Design and Analysis of Computed Tomographic Imaging Spectrometers (CTIS) Using Fourier and Wavelet Crosstalk Matrices by" (2010).
- [34] J. Qi, S. Member, and R. H. Huesman, "Wavelet Crosstalk Matrix and Its Application to Assessment of Shift-Variant Imaging Systems," 123–129 (2004).
- [35] M. Roumeliotis, R. Z. Stodilka, M. a Anastasio, G. Chaudhary, H. Al-Abed, E. Ng, A. Immucci, and J. J. L. Carson, "Analysis of a photoacoustic imaging system by the crosstalk matrix and singular value decomposition.," *Opt. Express* **18**(11), 11406–11417 (2010).

Chapter 2

2 Objective assessment of 3D photoacoustic tomography by the spatial crosstalk matrix

This chapter is based on a research paper in preparation for submission to the Journal of Biomedical Optics. The work presented here aimed to derive FoM for system performance from the spatial crosstalk matrix. The results suggested that these FoM could be used to objectively characterize PAT system performance and develop strategies for system optimization.

2.1 Introduction

2.1.1 Background

Photoacoustic tomography (PAT) is a hybrid imaging modality that combines the high spatial resolution of ultrasound imaging with the high-contrast of optical imaging [1]. It is based on the detection of ultrasound (US) waves generated by an object when exposed to laser light pulsed on the nanosecond timescale [2]. When an object is pulsed with laser light, a small fraction of energy is absorbed and emitted as a pressure wave due to the thermoelastic effect. The technique provides a means to estimate the optical properties of an object through acoustic detection of the US, which in turn provides information such as location, size, and function of the object [3]. Moreover, since the optical properties between tissue types generally differ to a greater degree than their mechanical and elastic properties, PAT can provide improved tissue delineation and specificity when compared to imaging techniques that use US or photon propagation alone [4]. Objects such as human arm vasculature [5], whole-body small animal vasculature [6], human breast cancer [7,8], brain in small animals [9,10], and many others have been successfully visualized by PAT.

2.1.2 PAT system design

Recently, several groups have reported development of real-time 3D PAT using a staring transducer array [11–13]. It is generally known that the performance of 3D PAT is dependent on the design of the staring transducer array; however, methods to systematically assess different designs are still lacking. Conventional metrics used to evaluate PAT system performance include sensitivity, resolution, and streak length, typically measured for a point source object [14]. These metrics, however, can be misleading in relation to PAT system design as they are typically measured after applying an image reconstruction algorithm to recover an image (usually a point source).

Photoacoustic tomography systems that are designed with multiple imaging tasks in mind may be better optimized with generic figures of merit (FoM) that do not depend on the specific imaging task or the specific selection of image reconstruction algorithm used. In our earlier work, a higher level metric based on the singular value decomposition (SVD) was presented [15]. The metric derived from the SVD was based on examining the singular value spectrum. The number of effective singular values was proportional to the number of coefficients (i.e. voxels) recoverable, but comparison between two imaging system setups would be ambiguous due to differences in singular vectors. Each imaging system would have its own SVD and would be represented by a different set of singular vectors. Thus, the recovery of N components between imaging systems could produce greatly varying images. Furthermore, calculating the singular value spectrum is computationally expensive and would be impractical for optimization tasks with larger system matrices, characteristic of 3D problems.

2.1.3 Fourier crosstalk matrix

The crosstalk matrix is used in this chapter as a technique to characterize particular features of our imaging system. For details, please refer to section 1.4.2.

2.1.4 Objective and approach

Generic assessment techniques are a desirable alternative for optimization of PAT system design. Our previous work aimed to develop metrics for PAT system characterization based on the SVD, but these metrics were difficult to implement as a basis for

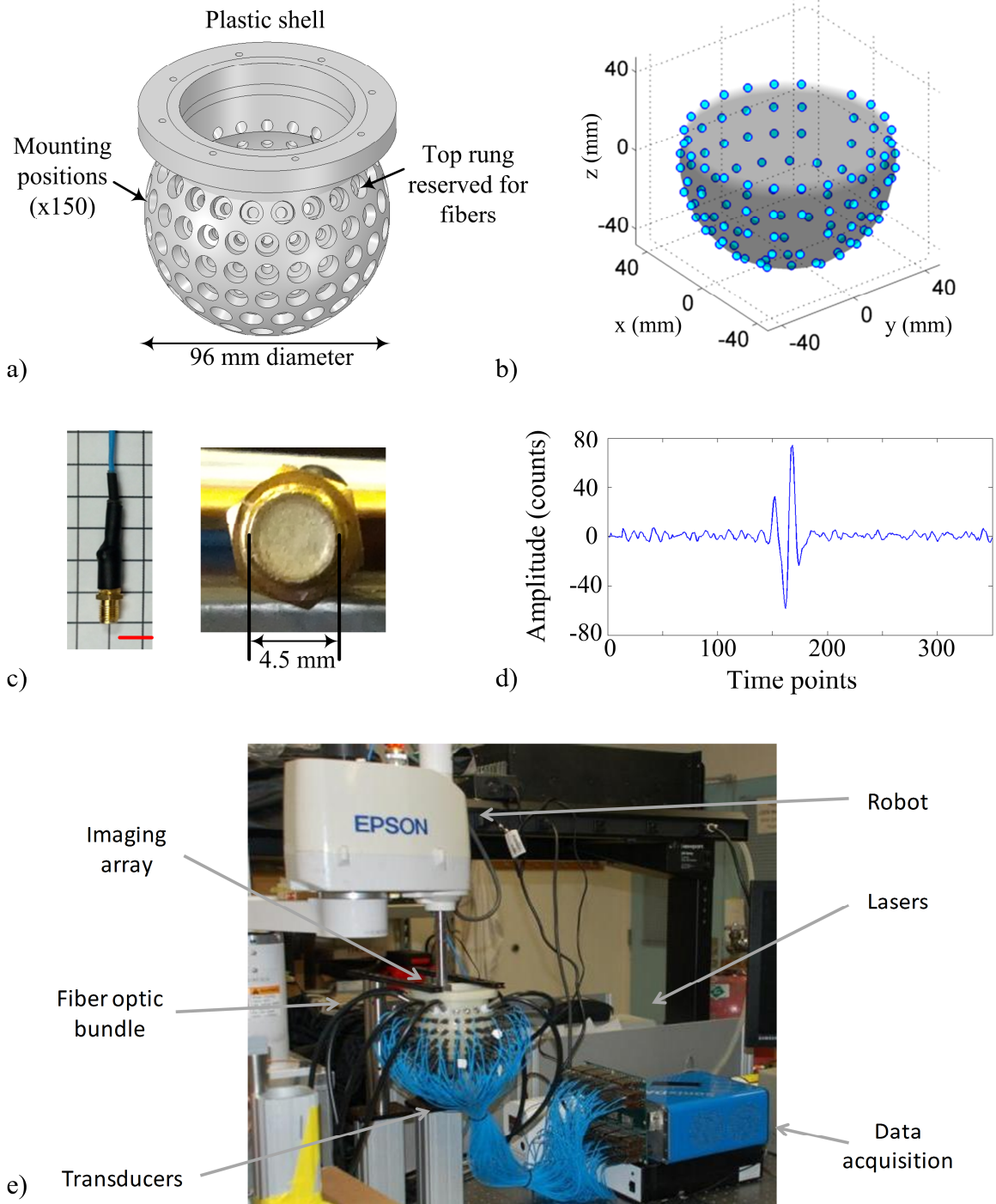
quantitative system optimization. The aim of this work was to explore more robust generic FoM for PAT system design assessment. The normalized spatial crosstalk matrix compared to the identity matrix was used to derive the FoM. The FoM considered were root mean square error (RMSE), peak signal-to-noise ratio (PSNR), mean absolute error (MAE), and a three dimensional structural similarity index (3D-SSIM). To our knowledge, this is the first time this approach, especially the use of 3D-SSIM derived from an experimentally constructed spatial crosstalk matrix, has been applied to objectively assess 3D PAT system design. The validity of the approach was tested by observing the response of the FoM as a function of transducer count and sampling rate. It is well understood in the field of PAT that system performance is proportional to transducer count and sampling rate [2,15,23]. Photoacoustic targets often appear surrounded by streaking artifacts, which are reduced in intensity as the number of projections (transducers) is increased [24]. The Nyquist rate refers to the lower bound of the sampling rate required for alias-free signals and is defined as twice the highest frequency within the signal. Sampling below the Nyquist rate results in image artifacts, due to folding over (i.e. aliasing) of higher frequency content into lower frequencies. Sampling above the Nyquist rate allows for greater signal fidelity. Therefore, the FoM were expected to improve as transducer count and sampling rate increased.

2.2 Materials and Methods

2.2.1 PAT system

The 3D PAT system utilized a plastic shell (Fig. 2-1(a)) designed to hold up to 150 transducers in a near-spherical staring arrangement. The inner surface of the shell had a radius of 48 mm. Transducer openings were located on 9 rungs evenly spaced along the zenith angle. The top rung was located at a zenith angle of 30° (relative to a horizontal plane intersecting the center of the shell) and each consecutive rung was spaced in 15° increments. Mounting positions for the transducers were spread azimuthally counter-clockwise to provide uniform coverage over 360° within each rung, such that there were 21, 24, 24, 24, 21, 17, 12, 6, and 1 mounting positions in the top to bottom rung,

respectively. The mounting position of the first transducer in each rung was longitudinally positioned at an azimuth angle of 0° . A total of 96 custom-built cylindrical unfocused transducers (2.7 MHz central frequency, ~127% bandwidth, 4.5 mm diameter) were mounted into the shell at all but the top rung as depicted in Fig. 2-1(b). A photograph of the transducer and an example transducer response are shown in Fig. 2-1(c)-(d). The Nyquist rate for the transducers was estimated to be approximately 16 MHz according to the bandwidth of the transducer (i.e. transducers were able to detect up to ~8 MHz). The top rung was reserved for laser illumination (Surelite II Nd:YAG, Continuum, Santa Clara, California), which was delivered through two, four-legged optical fiber bundles that were inserted to provide diffuse illumination (4 x 3 mm x 1000 mm quartz fiber with fused input, Lumen Dynamics, Mississauga, ON). For these experiments, the fibers were not used as no imaging was performed. Data acquisition was performed with a 128-channel analog-to-digital data acquisition system (12 bit resolution, 40 MHz sampling rate, SonixDAQ, Ultrasonix Medical Corp., Richmond, BC) that was triggered on the electronic Q-switch signal from the laser. Data acquisition and data transfer were controlled through the SonixDAQ demonstration software and image reconstruction and image display were performed offline with a custom script for MATLAB® (The Mathworks, Inc., version 7.8.0, Natick, Massachusetts). A photograph of the system is shown in Fig. 2-1(e).



2.2.2 Spatial crosstalk matrix

The photoacoustic image reconstruction problem can be expressed as a linear continuous-to-discrete model:

$$g = Hf + e \quad (2.1)$$

where \mathbf{g} represents the measured data set, H is the imaging operator (also referred elsewhere as the system matrix or forward model), f represents the unknown object(s), and e represents a noise process. The aim is to estimate f from the noisy data g but in most real situations the problem is ill-posed. A linear regularization procedure is usually applied in order to minimize estimation error. A robust regularization procedure aims to minimize the aliasing (i.e. linear dependencies) in H without compromising signal intensity. Aliasing that is not removed during the inversion process may appear in reconstructed images. Objective assessment of H , prior to the regularization procedure, provides insight into system design and here we propose to utilize the spatial crosstalk matrix to accomplish this task. The spatial crosstalk matrix can be expressed as:

$$B = H^T H \quad (2.2)$$

with elements defined by:

$$B_{jj'} = \sum_{k=1}^K (H_{jk}^T H_{j'k}) \quad (2.3)$$

where H^T represents the transpose of H , j and j' represent the index of the first and second voxel coefficient, k denotes the product of the time index for a given transducer and the index of the transducer, and K denotes the product of the total number time indices and the total number of transducers. Two important features can be derived from the spatial crosstalk matrix: system sensitivity and aliasing. The elements along the diagonal of the crosstalk matrix describe the system sensitivity, which is defined as the sum of the photoacoustic signal magnitude associated with each voxel in object space. Examination of the off-diagonal elements of the crosstalk matrix provides a measure of aliasing at each voxel. Aliasing represents the degree of overlap between the time series due to PA sources located at different voxels.

The spatial crosstalk matrix was computed according to Eq. (2.2) for each \mathbf{H} as a function of transducer count and temporal sampling rate. The transducer count was iterated from 8

to 96 transducers in increments of 8. Sampling rates of 5, 10, 20, and 40 MHz were used. The order in which mounting positions were defined around the bowl was used to guide transducer selection for a given transducer count. The mounting positions containing transducers were indexed from 1 to 96 counting counter-clockwise in each rung (from azimuth angle of 0°) starting with the second rung. For a transducer count of $8n$, where n is the iteration index ranging from 1 to 12, transducers with indices $12m + 1$ were selected, where m is 0, 1, ..., n . This selection algorithm was used to provide even coverage over object space. Each row of the crosstalk matrix was normalized and reshaped into the spatial dimensions of object space. The FoM were calculated in reference to the correspondingly reshaped identity matrix.

2.2.3 Calibration scan

The calibration scan involved experimentally measuring the PA time series (i.e. pressure modulations) due to PA sources in object space, thereby constructing \mathbf{H} . The calibration scan procedure has been described in previous work [22,25]. Briefly, light from a laser was guided through a 50- μm diameter optical fiber (Thorlabs, Newton, New Jersey). The output tip of the optical fiber was coated (Black Connector Coating, MG Chemicals, Burlington, Ontario). The coated tip acted as the photoacoustic point source and was mechanically fixed to the effector end of a SCARA robot arm (model E2C351S-UL with RC420 controller, Epson, Carson, California) to facilitate rapid and precise positioning. The input of the optical fiber was stripped of cladding and inserted into the 1064-nm beam of the laser. During calibration, the 4-legged optical fiber bundles were not used. Laser pulse energy was controlled by setting the Q-switch delay through software. A monitoring transducer (similar to one shown in Fig. 2-1(b)) was attached to the robot arm at a fixed position relative to the point source in order to monitor changes in signal amplitude over the scan duration. The monitoring transducer signal was acquired with the SonixDAQ in parallel with the 96 transducer signals from the array and used to correct for variations in the array-based signals due to the variability of the laser energy from pulse to pulse. An example of an averaged signal from the monitoring transducer acquired over 5 triggers is shown in Fig. 2-1(d). A scan volume of $20 \times 20 \times 20 \text{ mm}^3$ centered with respect to the transducer array was sampled with a 500- μm grid spacing

and 40-MHz temporal sampling rate (Fig. 2- 1(c)). The transducer signals due to each laser pulse were sampled for 25 μs (i.e. 1000 time points per transducer). The total size of the imaging operator was 96000 time points by 64000 grid points. The time to move the robot, fire the laser and capture the data took approximately 0.35 s per grid location and the entire scan took approximately 6 hours to complete.

The imaging operator was denoised using a filtering approach adapted from previous work [22]. Previously, the peak size, peak width and time of flight were estimated from the acquired imaging operator data for each transducer and grid location and an inverted parabola was fitted according to these parameters. The denoised imaging operator in the current study was constructed by zeroing measured imaging operator data outside a defined window centered upon the time of flight for each transducer and grid location. A window size of 61 time points was determined empirically by examining the nominal width of the pressure signals across all grid points and transducers. Although the inverted parabola closely resembled the velocity potential of the bipolar pressure signal, it did not account for minor ringing associated with the measured response of each transducer. We chose not to use a previously developed liquid-based point source since the methylene blue absorber tended to stain surfaces such as the front face of the fiber tip thereby introducing systematic variability in the measured transducer signals over time [26]. Additionally, signal amplitudes from the liquid point source tended to be weak in comparison to the coated fiber tip.

2.2.4 Figures-of-Merit

In the context of the spatial crosstalk matrix, the FoM utilized in this study are analogous to conventional image quality assessment (IQA) metrics. A common IQA image quality measure is root mean square error (RMSE) and is defined as

$$RMSE = \frac{1}{n} (\sum_{t=1}^n |e_t|^2)^{1/2} \quad (2.4)$$

where e_t is the estimation error and t represents the index of the voxel elements in the image. Here we also utilized the IQA measures peak signal-to-noise ratio (PSNR) and mean absolute error (MAE) to provide additional system information [27]. They are defined as

$$PSNR = 20 \log_{10} \left(\frac{MAX_I}{RMSE} \right) \quad (2.5)$$

$$MAE = \frac{1}{n} \sum_{t=1}^n |e_t| \quad (2.6)$$

where MAX_I is the maximum possible value of the image. These FoM are categorized as signal fidelity measures and are widely accepted due to their simplicity and clear physical meaning. By measuring the differences between the given images to a reference image, e_t is calculated. In this case, the reference images were represented by the diagonal and corresponding rows of the identity matrix (i.e. images with no aliasing). The RMSE score will always have higher values than MAE and is more sensitive to large errors within the model. The MAE is similar to RMSE but has advantages over RMSE as an estimator of model performance [28]. The RMSE and MAE can also be analyzed together to provide additional information regarding error distribution. Generally, if the difference between their values is small, the model makes many relatively small errors, whereas if the difference is large, the model makes few large errors. Both RMSE and MAE are negatively-oriented scores, whereas PSNR is a positively-oriented score.

In the field of IQA, it has been well acknowledged that signal fidelity measures do not match well with perceived visual quality (PVQ). Images with consistent RMSE or MAE values may have drastically different perceptual quality. Therefore, much effort has been placed in the development of PVQ metrics in order to approximate the human visual system, as it is the ultimate perceiver and appreciator of images. The structural similarity (SSIM) index is one of the most well cited PVQ metrics [29]. By comparing local patterns of pixel intensities, SSIM estimates image quality, or in this case system performance, as perceived changes in structural information [30]. The SSIM measure between two windows x and y of common size, where x is the windowed image and y is the windowed reference image, can be expressed as:

$$SSIM(x, y) = \frac{(2\mu_x\mu_y + C_1)(2\sigma_{xy} + C_2)}{(\mu_x^2 + \mu_y^2 + C_1)(\sigma_x^2 + \sigma_y^2 + C_2)} \quad (2.7)$$

where μ is the average, σ^2 is the variance, σ is the covariance and C_1 and C_2 are variables included to avoid instability when the denominator is very close to zero. We selected the default values used in [29] for C_1 and C_2 . The window is displaced on the image and the calculation is repeated until the full image is covered. Averaging the repeated

measurements gives the resulting SSIM value, where a value of 1 represents a perfect score (i.e. images are identical). The SSIM is not typically implemented on 3D images, but we adapted a 3D-SSIM method developed for video quality assessment (VQA) [31]. The 3D-SSIM metric for VQA was implemented on a data cube comprised of 2D images captured over time, whereas the data cube we analyzed was the 3D object space. We used a mean 3D-SSIM (3D-MSSIM) index to evaluate overall system performance.

2.3 Results

2.3.1 System sensitivity and aliasing

System sensitivity, aliasing for the center voxel (i.e. center grid point in the array), and aliasing for a voxel on the left edge of the scanned volume (i.e. grid point located 2 cm in the negative x-direction from the center grid point) are illustrated as image maps in Fig. 2- 2. The data in Fig. 2-2 is presented as a function of transducer count and sampling rate. For each condition, three z-planes near the center of object space (3.5 mm below the center plane, the center plane, and 3.5 mm above the center plane) are displayed. The system sensitivity maps in Fig. 2- 2(a) were independently normalized according to the peak system sensitivity per sampling rate. The system sensitivity maps in Fig. 2- 2(b) illustrate the last row of Fig. 2- 2(a) normalized to the peak system sensitivity across all sampling rates. System sensitivity was spatially-dependent with a spherical shape. The region with highest system sensitivity occurred near the center of the bowl and decreased with distance from the center. System sensitivity increased as transducer count and sampling rate increased (Fig. 2- 2(a) and (b)), with the highest sensitivity observed for the 96 transducers and 40 MHz sampling rate condition.

The aliasing maps displayed in Fig. 2- 2(c) and (d) were normalized to the peak amplitude per transducer count and per sampling rate in order to visualize changes in aliasing shape and pattern. At lower transducer counts and sampling rates, the aliasing pattern for the center and edge voxel appeared as streaks originating from the voxel position. As transducer count and sampling rate increased, streaking decreased. The trend

was also true as a function of spatial position, where the center voxel had the least amount of streaking. The differences in aliasing at higher transducer counts and sampling rates were not easily distinguished from the image maps.

Aliasing structure appeared to be inversely proportional to system sensitivity, as observed when comparing aliasing from the center voxel (Fig. 2- 2(b)) to an edge voxel (Fig. 2- 2(c)). At regions in object space with lower system sensitivity, such as the edge, aliasing appeared as streaks. In regions with higher system sensitivity, streaking was reduced and localized near the voxel. Aliasing structure appeared to transition from streaking to localized blurring as transducer count and sampling rate increased. Sampling rates that did not meet the Nyquist rate based on the transducer bandwidth resulted in aliasing maps corrupted with streaking patterns. However, artifacts in the system sensitivity maps computed for the lower sampling rates were not observably different from the system sensitivity map at Nyquist rate. Sampling above the Nyquist rate resulted in higher peak system sensitivity, but did not influence the aliasing maps substantially.

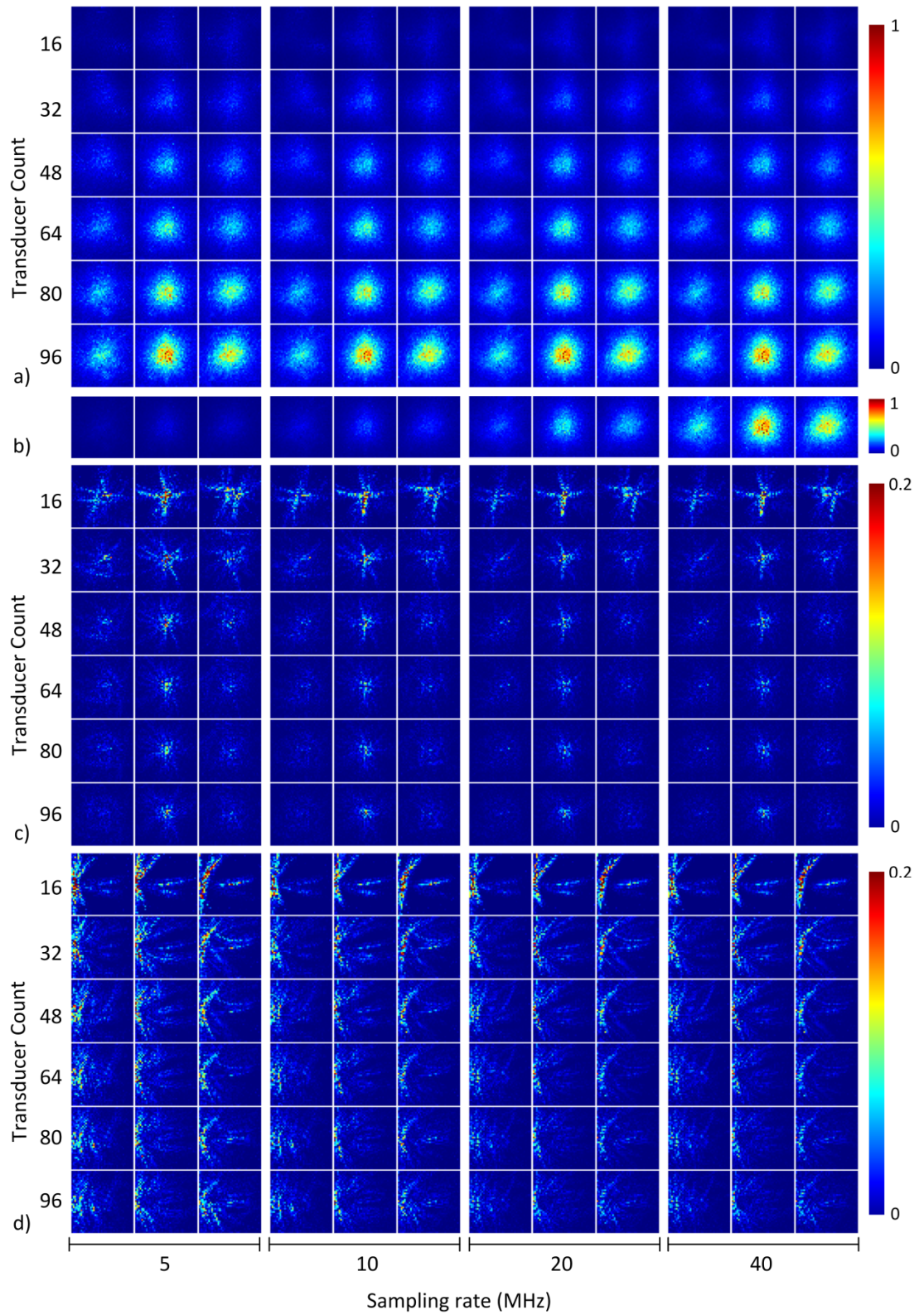


Figure 2-2 (a) System sensitivity maps of the z-plane 3.5 mm below center (left column), center plane (middle column), and z-plane 3.5 mm above center (right column) as a function of transducer count and sampling rate. Maps were normalized to peak system sensitivity per sampling rate. (b) System sensitivity

maps showing last row of (a) (96 transducers) normalized to peak system sensitivity across sampling rates. (c) Aliasing maps for the center voxel as a function of transducer count and sampling rate. Planes correspond to those shown in (a). Maps were normalized to peak system sensitivity per sampling rate and per transducer count and then scaled to 20% max for display purposes. (d) Same as (c) but for aliasing for a voxel near the edge of object space.

2.3.2 Figures-of-merit

The responses of the FoM as a function of transducer count and sampling rate are plotted in Fig. 2- 3. The changes at higher transducer counts and sampling rates that were difficult to visualize in the aliasing maps were quantified. The FoM plots exhibited improved scores as transducer count increased. The curves in each FoM plot were similar in shape, but the curves corresponding to 5 MHz and 10 MHz exhibited poorer scores than the 20 MHz and 40 MHz curves. Specifically, the 5 MHz and 10 MHz curves were approximately 10% and 5% metric score units poorer than the 20 MHz and 40 MHz scores at each transducer count. The curves in the signal fidelity FoM plots appeared to be somewhat exponential in shape, whereas the curves in 3D-MSSIM appeared to be substantially linear in shape. Furthermore, there was less overlap between the 20 MHz and 40 MHz curves in the 3D-MSSIM plot than in the other FoM plots. The spatially-dependent response of RMSE, MAE and 3D-MSSIM as a function of transducer count and sampling rate are illustrated as metric maps in Fig. 2- 4. The planes shown in Fig. 2- 4 correspond to those in Fig. 2- 2. The shape of the metric maps matched well with the spatially-dependent system sensitivity of the system and indicated optimal values in the center of object space. FoM scores also appeared to improve in the three planes as transducer count and sampling rate increased.

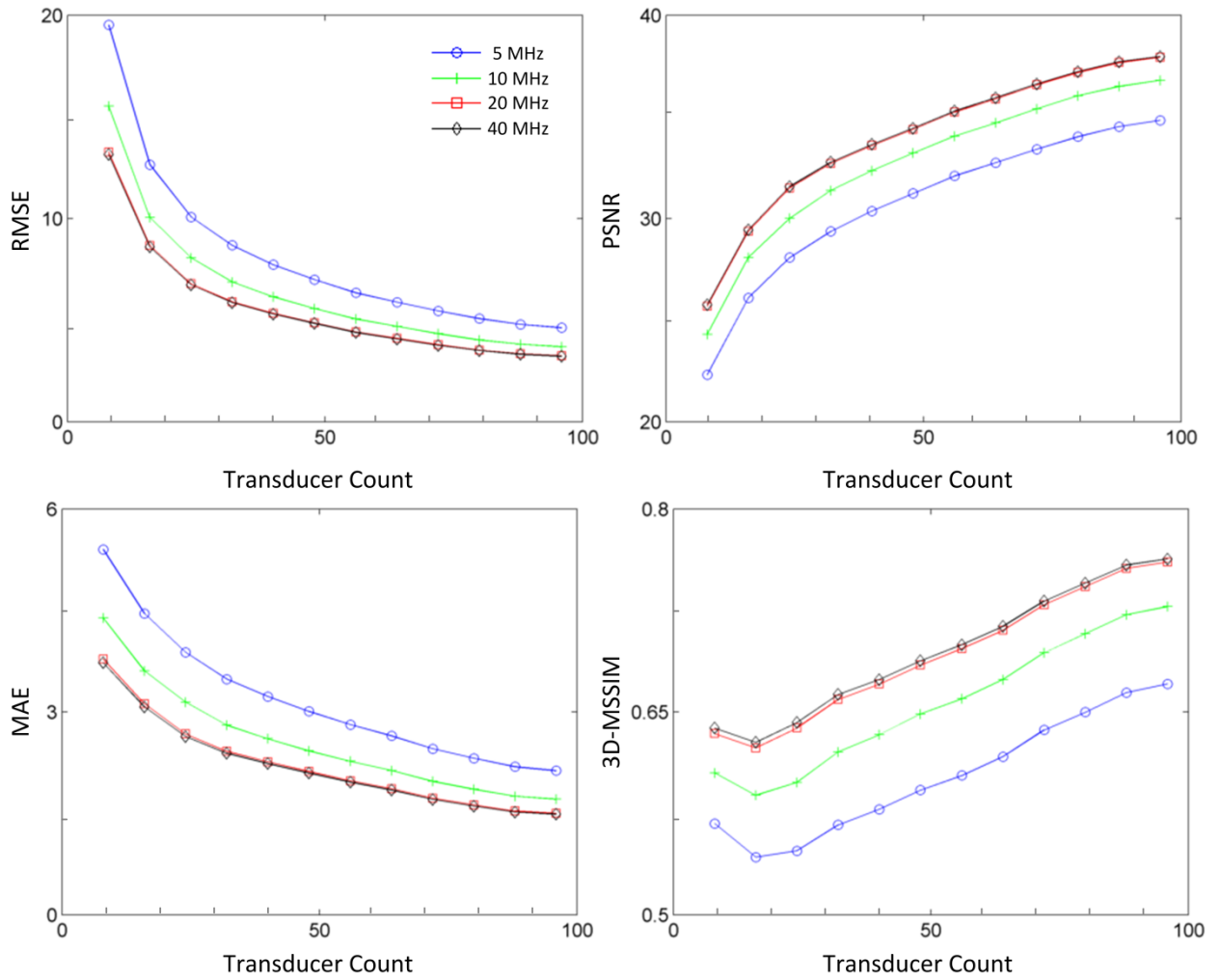


Figure 2-3 FoM for system performance (clockwise from top left: RMSE, PSNR, MAE, and 3D-MSSIM) plotted as a function of transducer count and sampling rate (legend shown in panel (a)).

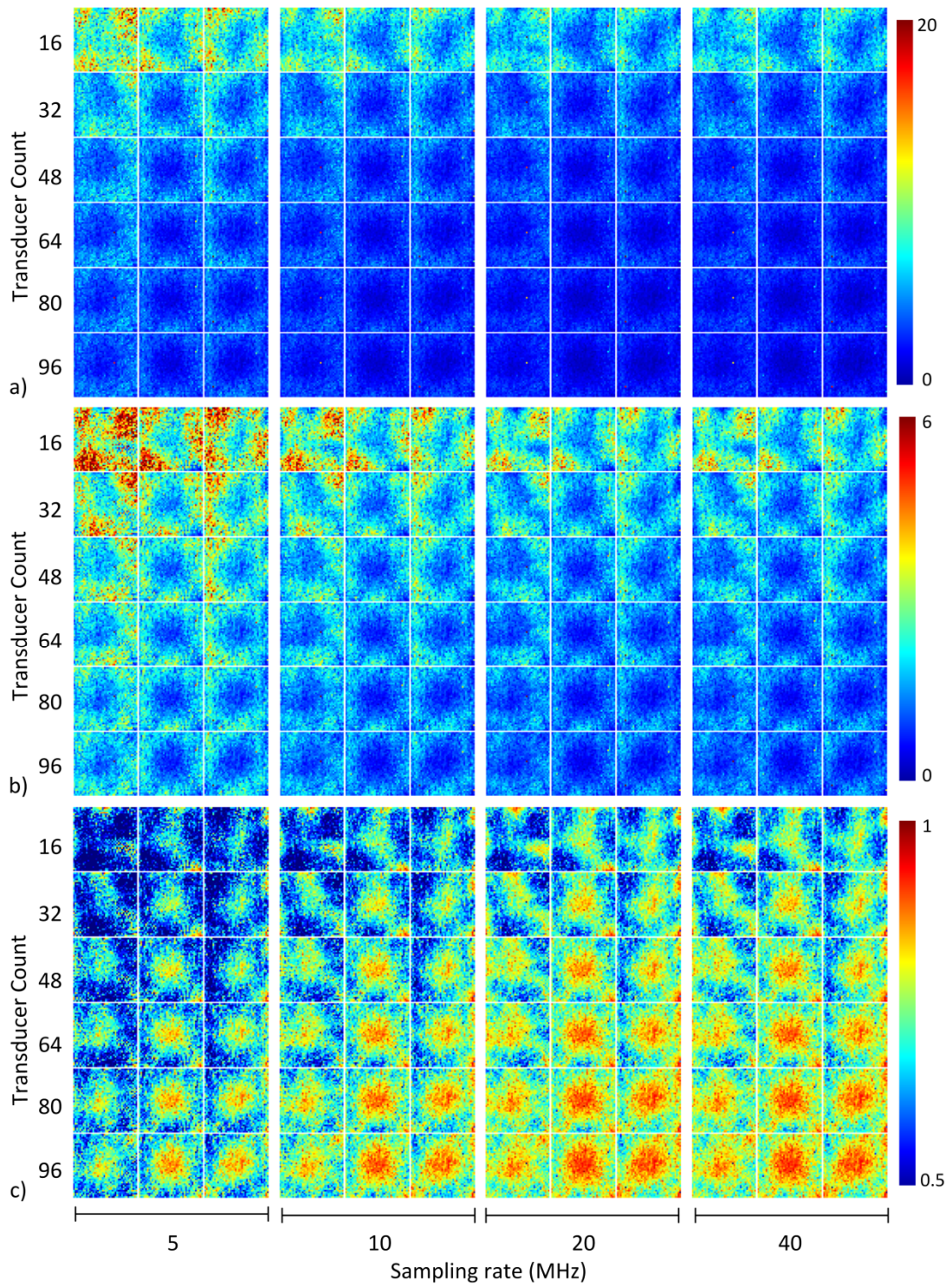


Figure 2-4 Metric maps for (a) RMSE, (b) MAE, and (c) 3D-MSSIM displayed as a function of transducer count and sampling rate in the z-plane 3.5 mm below center (left column), center plane (middle column), and z-plane 3.5 mm above center (right column).

2.4 Discussion

2.4.1 System sensitivity and aliasing

The PAT system we tested consisted of a 96-element near-spherical array with custom-built transducers. Improvements to the calibration process enabled acquisition of the system response with a finer resolution (500 μm) than our previous system (1.5 mm) and in a short period of time (~ 0.35 s per scan point versus 15 s per scan point). The improvement in resolution allowed for enhanced visualization and characterization of system response. As described in Sec. 1.4, increasing spatial and temporal sampling rate was expected to result in improved system performance. We observed that the spatial crosstalk matrix was capable of qualitatively representing the improvements related to increased transducer count and higher sampling rate for the 3D PAT system (Fig. 2- 2). System sensitivity increased and aliasing was reduced as transducer count and sampling rate increased. An increase in the transducer count corresponded to an increase in the number of intersecting arcs at a given point, which resulted in increased sensitivity. The higher number of intersecting arcs for higher transducer counts also explained the transition of the aliasing structure from heavily streaked at low transducer counts to a blurred spot, as the streaking artifacts were reduced at higher transducer counts. Signal aliasing occurred when signals were sampled below the Nyquist rate, which resulted in a greater number of streaking artifacts in the aliasing maps. Sampling rates of 20 MHz and 40 MHz were above the Nyquist rate, which allowed for alias-free signal detection. Therefore, system performance was nearly identical at the higher sampling rates. The spatial distribution of system sensitivity was spherical in shape with decreasingly sensitive concentric regions originating from the center (Fig. 2- 2(a)). This was expected from the near-spherical geometry of the array. Moreover, the directionality of the transducer faces, where each face was directed toward a common point at the center of the array, also gave rise to this spatial distribution of system sensitivity. Transducer angular sensitivity is relatively lower for PA signals arriving off-axis to the normal of the transducer face (i.e. the direction the transducer is facing) than signals arriving straight on. Thus, the center of the array had the highest spatial sampling.

2.4.2 Figures-of-merit

We have utilized generic FoM from the spatial crosstalk matrix for objective analysis of a 3D PAT system. The crosstalk elements displayed in Fig. 2- 2 were used to derive global FoM for system performance (Fig. 2- 3) as transducer count and sampling rate were manipulated. It is interesting to note that only 3D-MSSIM required the rows of the crosstalk and identity matrix to be reshaped into the dimensions of object space. Near-voxel dependencies were incorporated by 3D-MSSIM and then utilized to measure system performance according to the structure of the image. This may explain the difference in the shape of the curves between the signal fidelity FoM plots and the 3D-MSSIM plot. It can be argued that aliasing (i.e. streaking artifacts) in PAT is better represented by the structural information of the image rather than the overall quality of the image. Therefore, 3D-MSSIM would be more effective than signal fidelity FoM in detecting aliasing. The FoM were also visualized as metric maps (Fig. 2- 4) to examine local system performance. For both global and local system performance, the FoM aligned well with PAT sampling characteristics. As observed in Fig. 2- 3 and 4, the FoM scores improved with increasing spatial and temporal sampling rate. This suggested to us that the FoM derived from the spatial crosstalk matrix can be applied to characterize and optimize 3D PAT system design.

2.5 Conclusion

A PAT system consisting of a 96-element near-spherical array was built and PAT sampling characteristics were used to validate the spatial crosstalk matrix as a tool for quantitative 3D PAT system analysis. Figures-of-merit mirroring IQA metrics were derived from the spatial crosstalk matrix. The FoM used in this work were RMSE, PSNR, MAE and 3D-MSSIM. The response of the FoM were studied as a function of spatial and temporal sampling rate. Increasing spatial and temporal sampling rates (to the Nyquist rate) have been shown to result in improved PAT system performance. The response of the FoM matched these trends, suggesting they are useful for objectively characterizing

3D PAT system design as well as optimizing future design parameters, such as transducer arrangement, transducer directionality, and array shape.

2.6 Acknowledgments

Philip Wong and Ivan Kosik were supported by the Translational Breast Cancer Research Unit (TBCRU) as well as The University of Western Ontario (WGRS). Research funding was provided by the Canada Foundation for Innovation (CFI), the Natural Sciences and Engineering Research Council (NSERC), the Canadian Institute for Health Research (CIHR), The Ontario Ministry of Research and Innovation's Ontario Research Fund (ORF) through the Ontario Preclinical Imaging Consortium (OPIC), and the Lawson Health Research Institute (LHRI). MultiMagnetics Inc. provided matching funds with respect to ORF-OPIC.

2.7 References

- [1] C. Lutzweiler and D. Razansky, "Optoacoustic imaging and tomography: reconstruction approaches and outstanding challenges in image performance and quantification.," *Sensors (Basel)*. **13**(6), 7345–7384 (2013) [doi:10.3390/s130607345].
- [2] M. Xu and L. V. Wang, "Photoacoustic imaging in biomedicine," *Rev. Sci. Instrum.* **77**(4), 041101 (2006) [doi:10.1063/1.2195024].
- [3] S. Mallidi, G. P. Luke, and S. Emelianov, "Photoacoustic imaging in cancer detection, diagnosis, and treatment guidance.," *Trends Biotechnol.* **29**(5), 213–221, Elsevier Ltd (2011) [doi:10.1016/j.tibtech.2011.01.006].
- [4] P. Beard, "Biomedical photoacoustic imaging.," *Interface Focus* **1**(4), 602–631 (2011) [doi:10.1098/rsfs.2011.0028].
- [5] M. P. Fronheiser, S. a Ermilov, H.-P. Brecht, A. Conjusteau, R. Su, K. Mehta, and A. a Oraevsky, "Real-time optoacoustic monitoring and three-dimensional mapping of a human arm vasculature.," *J. Biomed. Opt.* **15**(2), 021305 (2010) [doi:10.1117/1.3370336].

- [6] H.-P. Brecht, R. Su, M. Fronheiser, S. a Ermilov, A. Conjusteau, and A. a Oraevsky, “Whole-body three-dimensional optoacoustic tomography system for small animals.,” *J. Biomed. Opt.* **14**(6), 064007 (2009) [doi:10.1117/1.3259361].
- [7] R. a. Kruger, R. B. Lam, D. R. Reinecke, S. P. Del Rio, and R. P. Doyle, “Photoacoustic angiography of the breast,” *Med. Phys.* **37**(11), 6096 (2010) [doi:10.1118/1.3497677].
- [8] S. a Ermilov, T. Khamapirad, A. Conjusteau, M. H. Leonard, R. Lacewell, K. Mehta, T. Miller, and A. a Oraevsky, “Laser optoacoustic imaging system for detection of breast cancer.,” *J. Biomed. Opt.* **14**(2), 024007 (2012) [doi:10.1117/1.3086616].
- [9] W. Lu, Q. Huang, G. Ku, X. Wen, M. Zhou, D. Guzatov, R. Su, A. Oraevsky, L. V Wang, et al., “Photoacoustic imaging of living mouse brain vasculature using hollow gold nanospheres,” *Biomaterials* **31**(9), 1–21 (2011) [doi:10.1016/j.biomaterials.2009.12.007.Photoacoustic].
- [10] X. Wang, G. Ku, M. a Wegiel, D. J. Bornhop, G. Stoica, and L. V Wang, “Noninvasive photoacoustic angiography of animal brains in vivo with near-infrared light and an optical contrast agent.,” *Opt. Lett.* **29**(7), 730–732 (2004).
- [11] L. Xiang, B. Wang, L. Ji, and H. Jiang, “4-D photoacoustic tomography.,” *Sci. Rep.* **3**, 1113 (2013) [doi:10.1038/srep01113].
- [12] B. Wang, L. Xiang, M. S. Jiang, J. Yang, Q. Zhang, P. R. Carney, and H. Jiang, “Photoacoustic tomography system for noninvasive real-time three-dimensional imaging of epilepsy.,” *Biomed. Opt. Express* **3**(6), 1427–1432 (2012) [doi:10.1364/BOE.3.001427].
- [13] P. Ephrat, L. Keenliside, A. Seabrook, F. S. Prato, and J. J. L. Carson, “Three-dimensional photoacoustic imaging by sparse-array detection and iterative image reconstruction.,” *J. Biomed. Opt.* **13**(5), 054052 (2010) [doi:10.1117/1.2992131].
- [14] A. Petschke and P. J. La Rivière, “Photoacoustic image reconstruction using the pseudoinverse of the system matrix with the potential for real-time imaging,” A. A. Oraevsky and L. V. Wang, Eds., 82233J (2012) [doi:10.1117/12.909145].

- [15] M. B. Roumeliotis, R. Z. Stodilka, M. a Anastasio, E. Ng, and J. J. L. Carson, “Singular value decomposition analysis of a photoacoustic imaging system and 3D imaging at 0.7 FPS.,” *Opt. Express* **19**(14), 13405–13417 (2011).
- [16] H. H. Barrett and H. Gifford, “Cone-beam tomography with discrete data sets.,” *Phys. Med. Biol.* **39**(3), 451–476 (1994).
- [17] H. H. Barrett, J. L. Denny, R. F. Wagner, and K. J. Myers, “Objective assessment of image quality. II. Fisher information, Fourier crosstalk, and figures of merit for task performance.,” *J. Opt. Soc. Am. A. Opt. Image Sci. Vis.* **12**(5), 834–852 (1995).
- [18] R. Z. Stodilka, E. J. Soares, and S. J. Glick, “Characterization of tomographic sampling in hybrid PET using the Fourier crosstalk matrix.,” *IEEE Trans. Med. Imaging* **21**(12), 1468–1478 (2002) [doi:10.1109/TMI.2002.806595].
- [19] J. F. Scholl, “The Design and Analysis of Computed Tomographic Imaging Spectrometers (CTIS) Using Fourier and Wavelet Crosstalk Matrices by” (2010).
- [20] J. Qi, S. Member, and R. H. Huesman, “Wavelet Crosstalk Matrix and Its Application to Assessment of Shift-Variant Imaging Systems,” 123–129 (2004).
- [21] P. Ephrat, M. Roumeliotis, F. S. Prato, and J. J. L. Carson, “Four-dimensional photoacoustic imaging of moving targets.,” *Opt. Express* **16**(26), 21570–21581 (2008).
- [22] M. Roumeliotis, R. Z. Stodilka, M. a Anastasio, G. Chaudhary, H. Al-Abed, E. Ng, A. Immucci, and J. J. L. Carson, “Analysis of a photoacoustic imaging system by the crosstalk matrix and singular value decomposition.,” *Opt. Express* **18**(11), 11406–11417 (2010).
- [23] A. Dima, N. C. Burton, and V. Ntziachristos, “Multispectral optoacoustic tomography at 64, 128, and 256 channels.,” *J. Biomed. Opt.* **19**(3), 36021 (2014) [doi:10.1117/1.JBO.19.3.036021].
- [24] M. Xu and L. Wang, “Universal back-projection algorithm for photoacoustic computed tomography,” *Phys. Rev. E* **71**(1), 016706 (2005) [doi:10.1103/PhysRevE.71.016706].

- [25] P. Ephrat and J. J. L. Carson, "Measurement of photoacoustic detector sensitivity distribution by robotic source placement," A. A. Oraevsky and L. V. Wang, Eds., 685610–685610–10 (2008) [doi:10.1117/12.763825].
- [26] M. Roumeliotis, P. Ephrat, J. Patrick, and J. J. L. Carson, "Development and characterization of an omni-directional photoacoustic point source for calibration of a staring 3D photoacoustic imaging system," *Opt. Express* **17**(17), 15228 (2009) [doi:10.1364/OE.17.015228].
- [27] W. Lin and C.-C. Jay Kuo, "Perceptual visual quality metrics: A survey," *J. Vis. Commun. Image Represent.* **22**(4), 297–312, Elsevier Inc. (2011) [doi:10.1016/j.jvcir.2011.01.005].
- [28] C. Res, C. J. Willmott, and K. Matsuura, "Advantages of the mean absolute error (MAE) over the root mean square error (RMSE) in assessing average model performance," 79–82 (2005).
- [29] Z. Wang, A. C. Bovik, H. R. Sheikh, and E. P. Simoncelli, "Image quality assessment: from error visibility to structural similarity.," *IEEE Trans. Image Process.* **13**(4), 600–612 (2004).
- [30] D. Brunet, E. R. Vrscay, and Z. Wang, "On the mathematical properties of the structural similarity index.," *IEEE Trans. Image Process.* **21**(4), 1488–1499 (2012) [doi:10.1109/TIP.2011.2173206].
- [31] I. I. Conference and I. Processing, "3D-SSIM FOR VIDEO QUALITY ASSESSMENT Kai Zeng and Zhou Wang," 1–4 (2012).
- [32] J. G. Bolaños, V. Pulkki, P. Karppinen, and E. Hægström, "An optoacoustic point source for acoustic scale model measurements.," *J. Acoust. Soc. Am.* **133**(4), EL221–7 (2013) [doi:10.1121/1.4793566].
- [33] S. Bu, Z. Liu, T. Shiina, K. Kondo, M. Yamakawa, K. Fukutani, Y. Someda, and Y. Asao, "Model-based reconstruction integrated with fluence compensation for photoacoustic tomography.," *IEEE Trans. Biomed. Eng.* **59**(5), 1354–1363 (2012) [doi:10.1109/TBME.2012.2187649].

Chapter 3

3 Design improvement of a staring, sparse transducer array for 3D photoacoustic tomography using the spatial crosstalk matrix

This chapter is based on a research paper in preparation for submission to Journal of Biomedical Optics. The work presented here demonstrated that the design of our current 3D PAT staring array system could be improved by optimizing different design parameters. The design strategies developed hold potential in improving system performance for any PAT staring array system.

3.1 Introduction

3.1.1 Background

Photoacoustic tomography (PAT) is a biomedical imaging modality capable of mapping optical absorption in tissues [1]. It is a hybrid technique that combines the high spatial resolution of ultrasound imaging with the high-contrast of optical imaging. When an object is exposed to modulated electromagnetic radiation, usually pulsed on the nanosecond timescale, an instantaneous elevation in temperature causes a pressure rise within the object, thereby generating acoustic waves in the surrounding medium [2]. By exploiting this phenomenon, the potential of PAT for biomedical imaging has been demonstrated through its ability to visualize a wide variety of structures and physiological parameters, including vasculature in the human arm [3], human breast lesions [4], brain in small animals [5, 6], blood flow [7], and blood oxygenation [8]. The imaging performance for a given PAT system is heavily dependent on how well the photoacoustic (PA) signals generated from an object are detected. Signal fidelity is generally determined by the sensitivity and bandwidth of the transducer array as well as the number of projections captured [9]. Many PAT systems have been built where a single transducer, or an array of transducers, is mechanically scanned around an object to capture the data needed to reconstruct a 3D image. Although a large number of

projections can be captured in this way, there is a trade-off between temporal resolution and image quality. Arising from the desire for fast real-time 3D PAT, several groups have begun to implement systems with staring transducer arrays [10-13], where image acquisition is limited only by the repetition rate of the laser. There has been much research on optimization of the temporal resolution for PAT systems that use mechanical scanning, but little emphasis on optimizing coverage for staring transducer arrays for a given transducer type. In this work, we examined different design parameters of a staring sparse array for a 3D PAT system in order to improve overall system coverage.

3.1.2 Crosstalk matrix

The crosstalk matrix is used in this chapter as a technique to characterize particular features of our imaging system. For details, please refer to section 1.4.2.

3.1.3 Objective and Approach

Our earlier work focused on optimization of the temporal resolution of 3D PAT imaging and a system was developed capable of capturing a single 3D PA image per laser pulse [10]. In this work, we endeavored to objectively study methods to improve imaging performance of a 3D PAT system without resorting to mechanical scanning methods. We studied the effect of acoustic coverage (i.e. spatial sampling) for a given transducer type and a fixed number of transducers. The effects of transducer arrangement, transducer array angular coverage, and transducer array radius on system performance were estimated through a series of simulations and quantified using FoM derived from the spatial crosstalk matrix.

3.2 Materials and Methods

For a detailed treatment of the spatial crosstalk matrix concept and the FoM used in this study, please refer to sections 2.2.2 and 2.2.4.

3.2.1 Simulations: 3D PAT system

The 3D PAT system simulated in this work was modeled after the experimental 3D PAT system introduced in our previous work [14]. The simulated 3D PAT system consisted of

a near-spherical shell of radius 47.5 mm and incorporated 129 transducers positioned tangentially to the surface of the shell. Transducers were spread across 8 rungs, where each rung was evenly spaced by 15° along the zenith (Φ) from -90° to 15° . The origin of the coordinate system was positioned at the center of the bowl, with the z-axis running tangential to the surface opening of the shell. The top boundary of the shell corresponded to $\Phi = 15^\circ$. Transducers were distributed along the bottom to top rung in counts of 1, 6, 12, 17, 21, 24, 24, and 24, respectively. Within each rung, transducers were spread azimuthally (θ) counter-clockwise to provide uniform coverage over 360° , where the first transducer in each rung was positioned at $\theta = 0^\circ$. For purposes of further discussion below, the transducer arrangement described above will be referred to as the *experimental transducer arrangement*. The transducer signal used in the simulations (Fig. 3- 1(a)) was the experimentally measured response of a custom-built unfocused ultrasound transducer (2.7 MHz central frequency, $\sim 127\%$ bandwidth, 4.5 mm diameter sensing element) to a PA point source [15]. Object space was defined as a cube 2 cm on edge located at the center of the transducer array comprised of grid points spaced 1 mm apart in a cubic arrangement. For each grid point in object space, the transducer response was amplitude-scaled and time-shifted to account for the angle (with respect to the normal to the sensing element) and distance between the center of the transducer and the grid point. The amplitude-scaling values, w , were determined experimentally by modeling the transducer response as a function of angle and distance. The values were expressed as

$$w = (0.0325 + 0.768^\alpha) * 2/d \quad (3.1)$$

where α represents the angle between the grid point and the normal to the surface of the transducer face and d is the distance between the center of the transducer and the grid point. The speed of sound was assumed to be 1500 m/s for all simulations. All simulations were run in MATLAB® (The Mathworks, Inc., version 7.8.0, Natick, Massachusetts).

3.2.2 Simulations: system design improvements

System coverage (i.e. the aggregate transducer response) with respect to object space was expected to depend on the transducer arrangement, angular coverage of the transducer array, and radius of the transducer array. Therefore, parameter searches were performed through a series of simulations. For the first simulation, transducer arrangement was treated as a Tammes problem [16]. The Tammes problem refers to the placement of a given number of points, N , on the surface of a sphere such that the minimum distance between points is maximized [17]. In our case, the placement of points corresponded to transducer positions ($N = 129$) and the Tammes problem was constrained to the surface of the shell (i.e. $\Phi = 15^\circ$). The resulting transducer arrangement was referred to as the *uniform sampling arrangement*. The second simulation evaluated system performance as a function of angular coverage of the transducer array and was similar to the first simulation. Transducer arrangement solutions to the Tammes problem using 129 transducers constrained to $\Phi = 0^\circ, 15^\circ, 30^\circ, 45^\circ$, and 60° for the shell were tested. Note that $\Phi = 0^\circ$ represented a hemispherical shell and $\Phi = 15^\circ$ represented the shape of the experimental transducer arrangement. The third simulation evaluated system performance as a function of radius of the sensing surface. The radius was varied from 37.5 mm to 87.5 mm in increments of 10 mm. Transducers were positioned using solutions to the Tammes problem and the shell was fixed at $\Phi = 15^\circ$.

The spatial crosstalk matrix was computed according to Eq. (2) for each system design and FoM were derived according to Eq. (4) – (7). Reference image maps were obtained by reshaping the corresponding rows of the identity matrix. The FoM were plotted as a function of concentric cubic shells in order to provide better insight into the spatial-dependent response of each system design. The cubic shells were assigned values from 1 to 10 according to their distance from the center of object space, where the innermost cubic shell was assigned the value 1 and the outermost cubic shell was assigned the value 10. The median for a given metric was calculated for the group of voxels located in a given cubic shell.

3.3 Results

3.3.1 System design parameters: spatial crosstalk elements

The experimental transducer arrangement and the uniform sampling arrangement are illustrated in the point cloud representations in Fig. 3- 1(b) and (c). From the point cloud representations in Fig. 3- 1(c), the pattern of transducers surrounding a given transducer appeared to be square-shaped for the experimental transducer arrangement and hexagonal for the uniform sampling arrangement. System sensitivity, aliasing for the center voxel (i.e. center grid point of the array), and aliasing for a voxel on the left edge (i.e. grid point located 2 cm from the center in the negative x-direction) are displayed as image maps for both transducer arrangements in Fig. 3- 1(d)-(f). The image maps show equally-spaced xy-planes for object space, where image maps arranged left to right correspond to planes from the bottom to top of object space. The system sensitivity maps in Fig. 3- 1(d) were normalized to the peak system sensitivity. The peak system sensitivity in both arrangements was observed at the center of object space. System sensitivity appeared identical for both arrangements, where system sensitivity was spherically-shaped and spatially-dependent (decreased proportionally with distance from the center). The uniform sampling arrangement appeared to have a more uniform system sensitivity response compared to the experimental transducer arrangement. The differences between the two transducer arrangements were more apparent in the aliasing maps (Fig. 3- 1(e) and (f)). Aliasing maps for the transducer arrangements were independently normalized to the peak amplitude. The aliasing maps for the center and edge voxel appeared to have fewer streak artifacts for the uniform sampling arrangement compared to the experimental transducer arrangement. Fig. 3- 2(a) and (b) display the point cloud representations of the system designs used to test angular coverage. The image maps in Fig. 3- 2(c)-(e) correspond to the xy-planes displayed in Fig. 3- 1(d)-(f). System sensitivity and aliasing maps were normalized according to the method used in Fig. 3- 1. Differences in system sensitivity and aliasing for the different cut-off angles of coverage were small and hence not easily visualized in the figure panels, but system sensitivity in the lower and upper planes representative of object space appeared to differ slightly across the cut-off angles of coverage. The point cloud representations and system

sensitivity and aliasing maps for the system designs as a function of array radius are illustrated in Fig. 3- 3. System sensitivity and aliasing maps were normalized according to the method used in Fig. 3- 1. As array radius increased, system sensitivity decreased and aliasing increased. System sensitivity in the lower planes of object space, however, had greater spatial variation as array radius decreased.

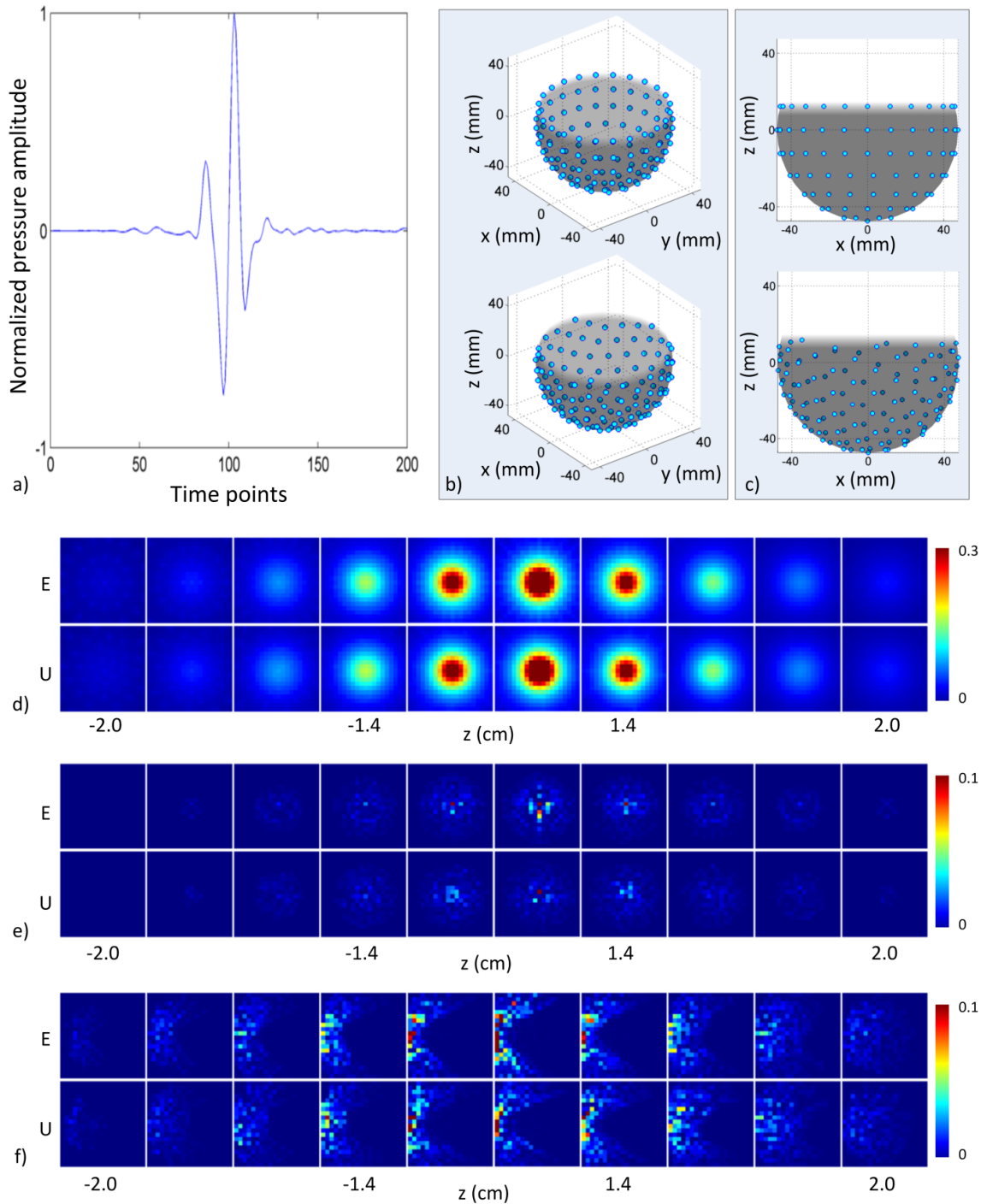


Figure 3-1 (a) Transducer response profile to a PA point source ($\sim 70\text{-}100\ \mu\text{m}$) averaged over 64000 triggers acquired with one transducer at 40 MHz sampling rate. The amplitude represents the counts on the digital converter and has been normalized to the max sensitivity. (b) Point cloud representations of the experimental transducer arrangement (top) and uniform sampling arrangement (bottom). Darker shaded area represents exterior of shell closest to reader. Lighter shaded area represents interior surface of the shell. (c) Same as (b) from a side-view. (d) Normalized sensitivity maps for the two arrangements and scaled to 30% max sensitivity for display purposes. Aliasing maps for the center voxel (e) and a voxel along the left edge (f) shown for the two arrangements (experimental transducer arrangement in the top row and uniform sampling arrangement in the bottom row). Each arrangement was independently normalized and scaled to 10% max for display purposes. The image planes are $2 \times 2\ \text{cm}^2$ and correspond to every other xy-plane of object space (left to right corresponds to bottom ($z = -2\ \text{cm}$) to top ($z = 2\ \text{cm}$) planes at 1 mm step size).

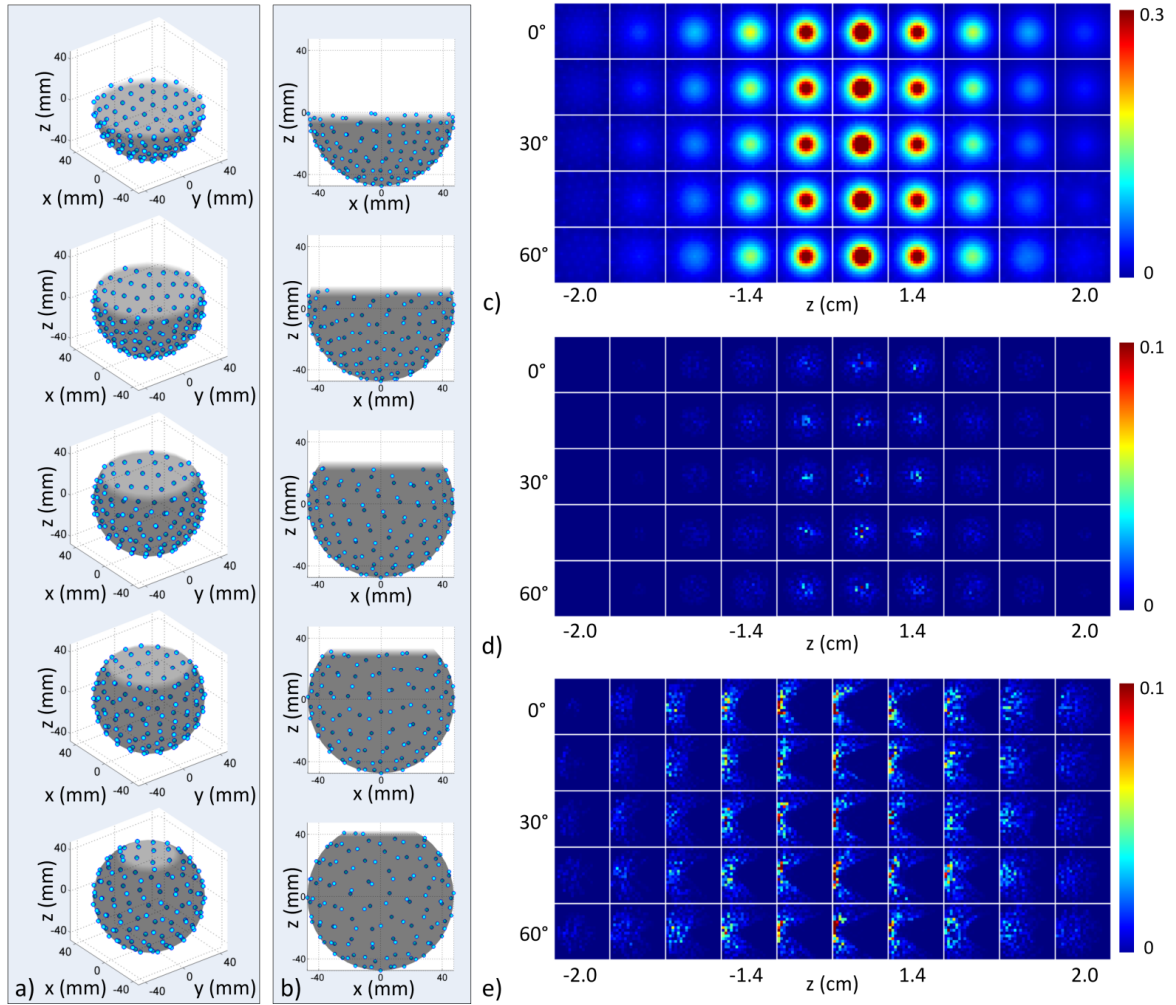


Figure 3-2 (a) Point cloud representations of transducer arrays as a function of array angular coverage (top to bottom corresponds to 0° to 60°). (b) Same as (a) but from a side view. (c) Normalized sensitivity maps (scaled to 30% max for display purposes) for each array coverage angle (top to bottom row corresponds to 0° to 60°). (d) Independently normalized aliasing maps (scaled to 10% max for display purposes) for the center voxel and left edge voxel (e) for each array coverage angle. Image planes correspond with those in Fig. 3-1.

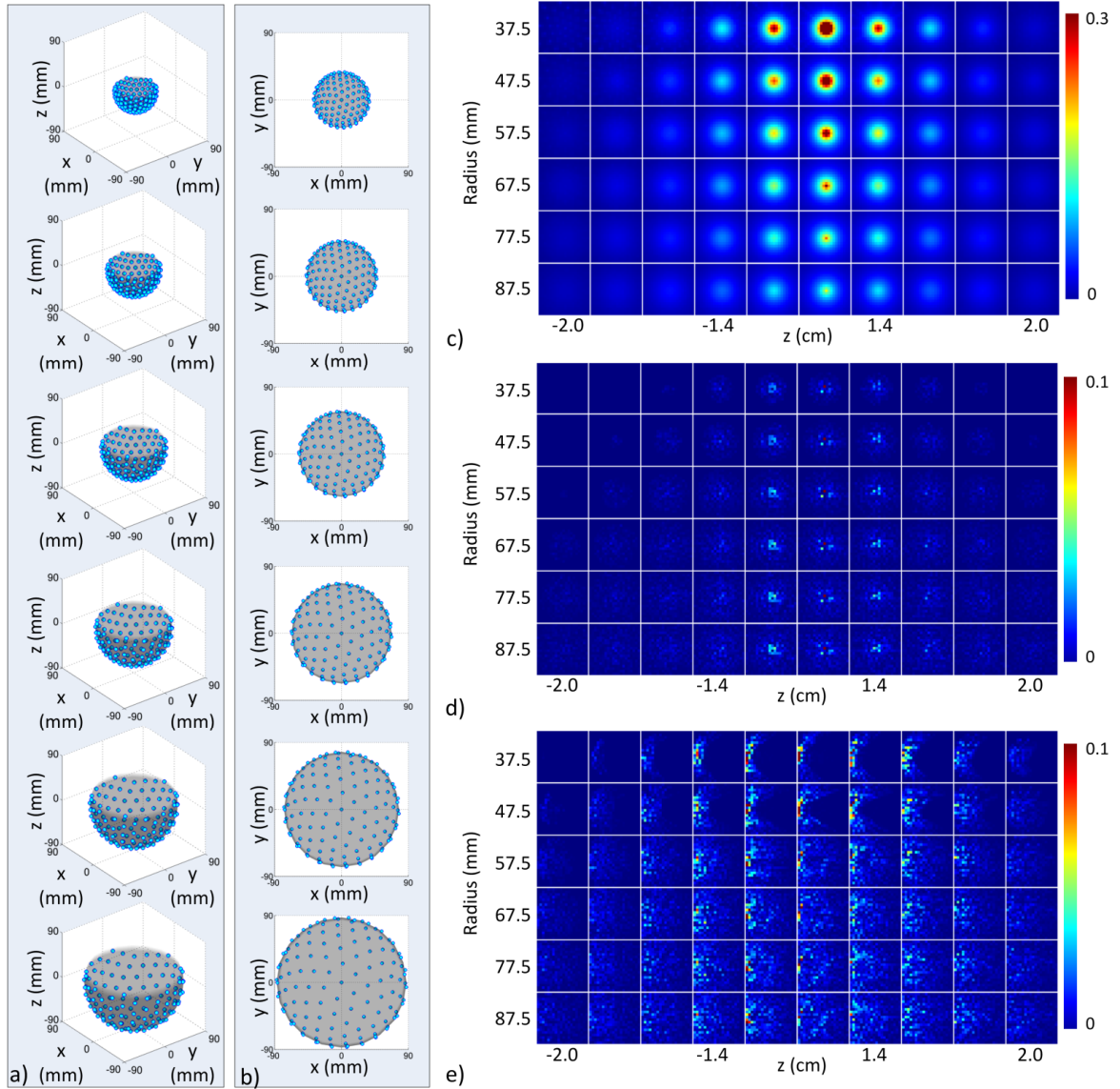


Figure 3-3 (a) Point cloud representations of transducer array as a function of array radius (top to bottom corresponds to 37.5 mm to 87.5 mm). (b) Same as (a) but from the top view. (c) Normalized sensitivity maps (scaled to 30% max for display purposes) for each array radius (top to bottom corresponds to 37.5 mm to 87.5 mm, respectively). (d) Independently normalized aliasing maps (scaled to 10% max for display purposes) for the center voxel and left edge voxel (e) for each array radius. Image planes correspond with those in Fig. 3-1.

3.3.2 System design assessment: FoM

The FoM for the first test are shown in Fig. 3- 4. The uniform sampling arrangement produced better scores than the experimental transducer arrangement in all FoM maps (Fig. 3- 4(a)), particularly in the center of object space. The shape of the figure-of-merit maps for both arrangements was spherical in shape. Both arrangements exhibited similar curves when plotted as a function of concentric cubic shells (Fig. 3- 4(b)). The uniform sampling arrangement exhibited better scores than the experimental transducer arrangement at each concentric cubic shell. The FoM for the second test are shown in Fig. 3- 5. System response was almost identical across the different cut-off angles of coverage, but slight differences were apparent in the lower and upper planes of object space. As the cut-off coverage angles increased, system response showed poorer scores near the bottom and top of object space. The shape of the curves for all FoM was similar to those in Fig. 3- 4(b). Fig. 3- 6 displays the FoM for the third test. The FoM maps again appeared to be spherical in shape. With decreasing array radius, voxel-to-voxel variation increased in the outer cubic shells. From the RMSE and PSNR plots, the curves intersected at the 6th cubic shell, corresponding to an object space size of 1.2 cm x 1.2 cm x 1.2 cm. The planes in the FoM maps shown in Fig. 3- 4 to Fig. 3-6 correspond to those in Fig. 3-1 to Fig. 3-3.

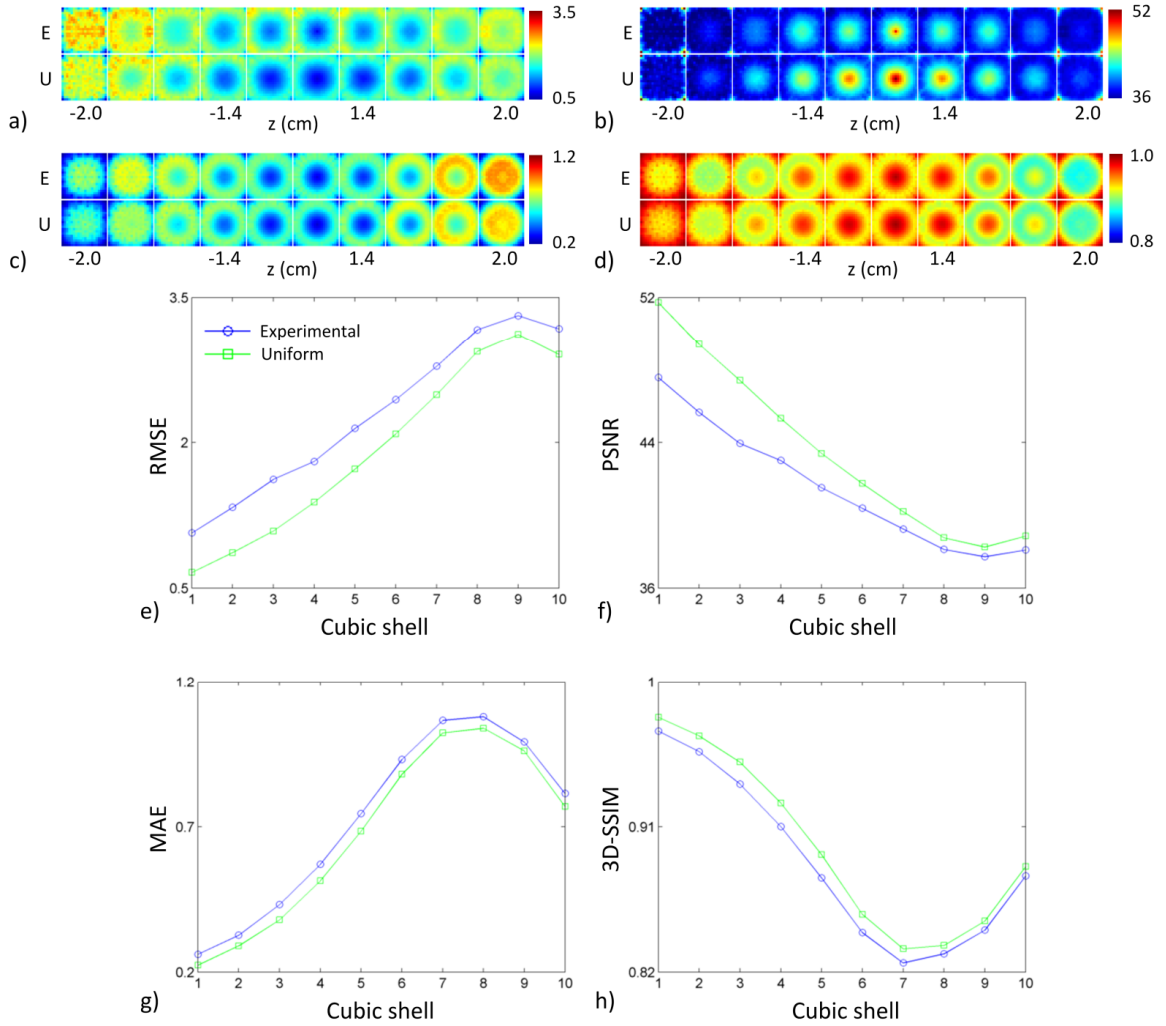


Figure 3-4 Metric maps for (a) RMSE, (b) PSNR, (c) MAE, and (d) 3D-SSIM displayed for both experimental transducer arrangement (top row) and uniform sampling arrangement (bottom row). (e)-(h) System performance figures of merit (RMSE, PSNR, MAE, and 3D-SSIM reading clockwise starting from top left panel) plotted as a function of cubic shells for the two arrangements (legend shown in panel (e)).

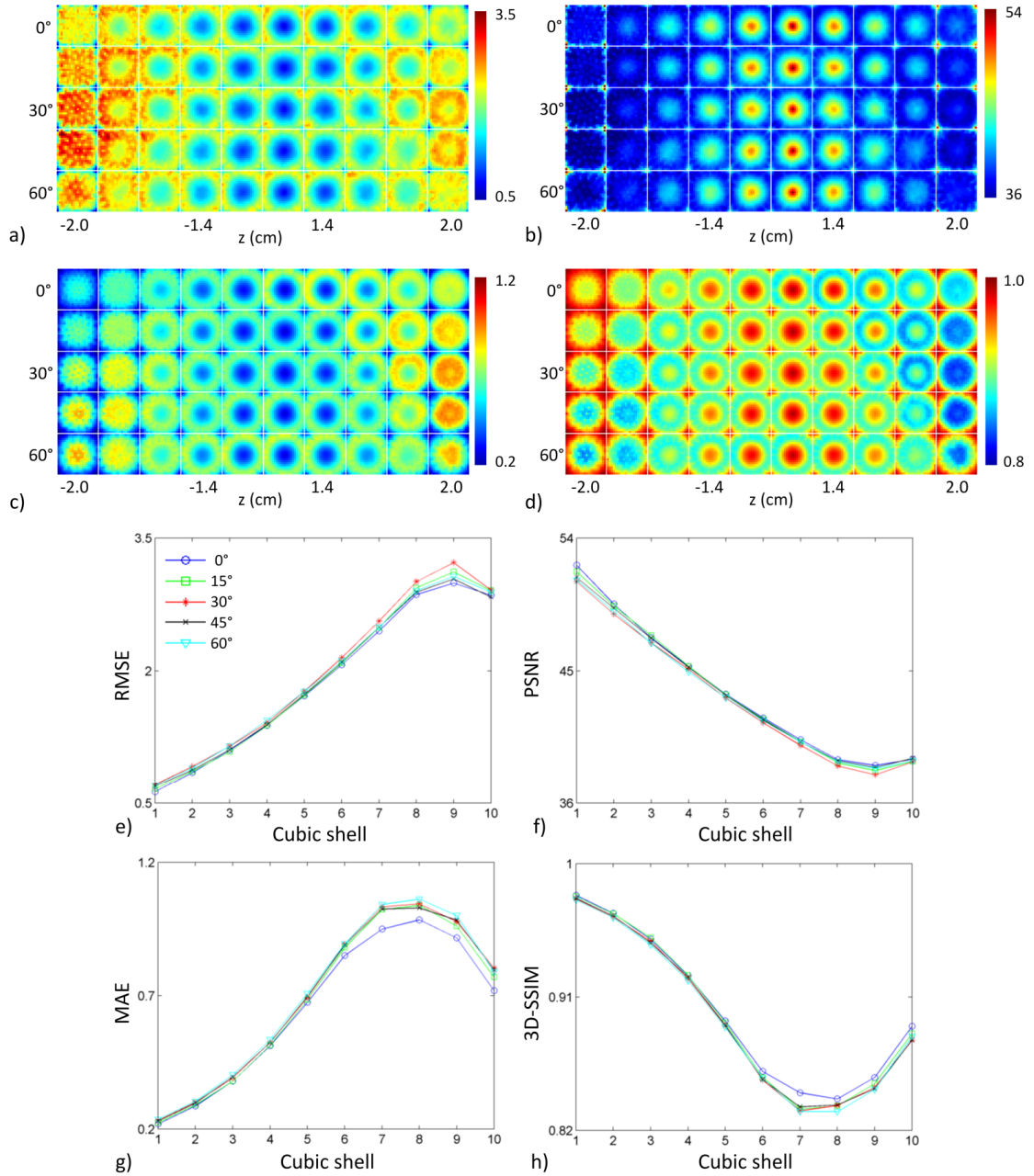


Figure 3-5 Metric maps for (a) RMSE, (b) PSNR, (c) MAE, and (d) 3D-SSIM displayed as a function of array angular coverage (top to bottom corresponds to 0° to 60°). (e)-(h) System performance figures of merit (RMSE, PSNR, MAE, and 3D-SSIM reading clockwise starting from top left panel) plotted as a function of cubic shells with varying array angular coverage (legend shown in panel (e)).

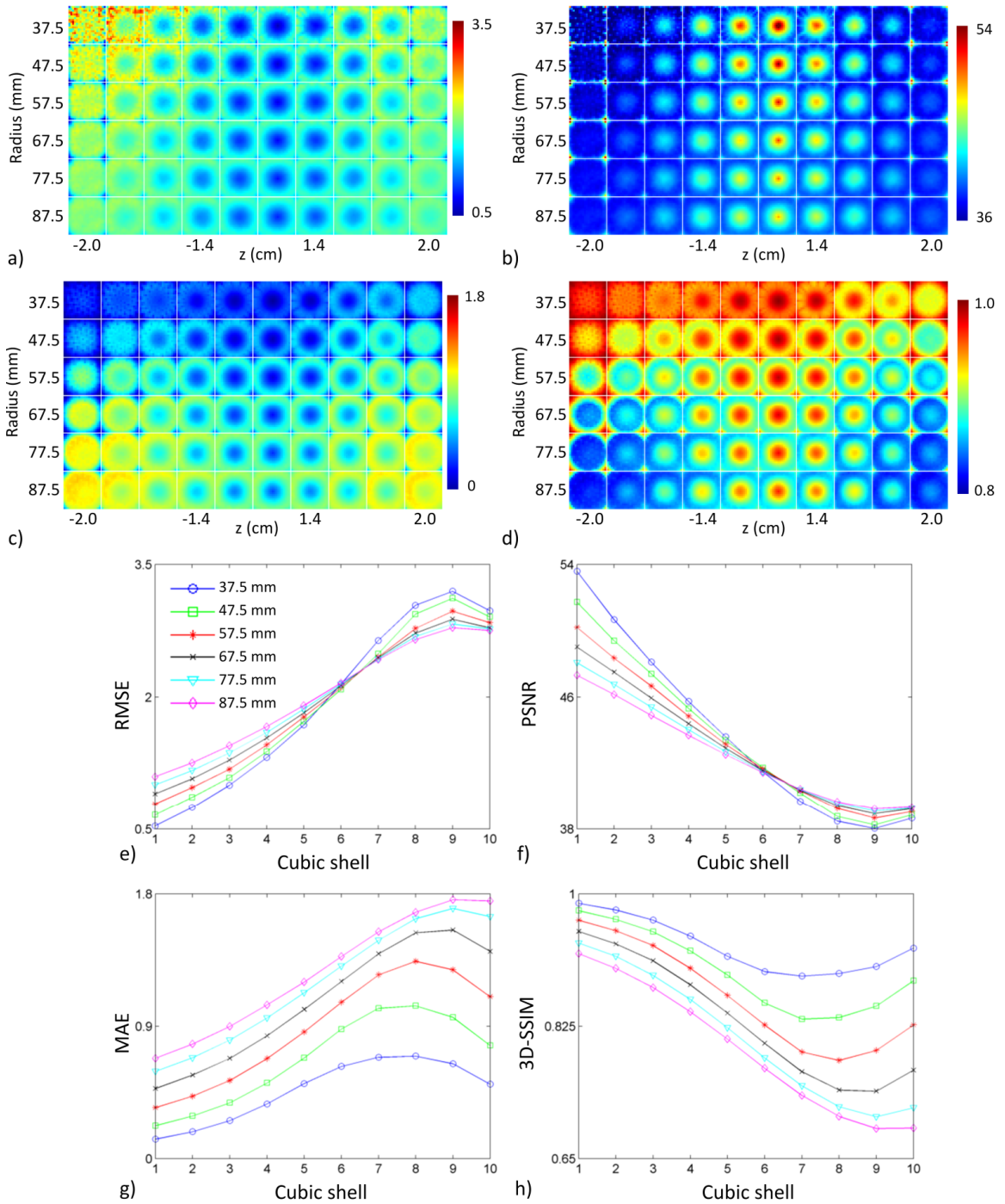


Figure 3-6 Metric maps for (a) RMSE, (b) PSNR, (c) MAE, and (d) 3D-SSIM displayed as a function of array radius (top to bottom corresponds to 37.5 mm to 87.5 mm). (e)-(h) System performance figures of merit (RMSE, PSNR, MAE, and 3D-SSIM reading clockwise starting from top left panel) plotted as a function of cubic shells with varying array radius (legend shown in panel (e)).

3.4 Discussion

3.4.1 System coverage

With a fixed number of transducers, the transducer array coverage was examined by estimating the effects of transducer arrangement, array angular coverage, and array radius. The arrangement of transducers on the experimental system provided uniform coverage azimuthally within each rung but sub-optimal coverage along the zenith (top of Fig. 3- 1(c)). A more uniform distribution of transducers on the bowl was obtained by solving the Tammes problem (bottom of Fig. 3- 1(c)). The increase in coverage along the zenith accounted for the increase in uniformity of the system sensitivity (Fig. 3- 1(d)) as well as a decrease in aliasing (Fig. 3- 1(e) and (f)). System sensitivity and aliasing did not appear to change as a function of the cut-off angle of the array in the Φ direction. This was likely due to the fact that the number of projections acquired was still determined by the number of transducers and that the projections were uniformly distributed. System sensitivity decreased and aliasing increased as a function of array radius (Fig. 3- 3). System sensitivity also became more uniform with larger array radii. Positioning transducers farther away from the object space would increase the number of object grid points falling within the transducer acceptance angle, but reduce overall system sensitivity (Eq. (8)).

3.4.2 System design assessment

Deriving FoM from the spatial crosstalk matrix enabled an objective assessment of the sparse detection problem. Each spatial crosstalk matrix represented a different sparse detection design and was evaluated in reference to the identity matrix, representing a shift-invariant, full-view system. The off-diagonal elements of the crosstalk matrix represented the instability that arises from sparse detection and the FoM assessed how closely aligned a system design was to the ideal full-view system. The improved performance of the uniform sampling arrangement was quantified in Fig. 3- 4. The uniform sampling arrangement was shown to outperform the current transducer arrangement in every cubic shell of object space. The shape of the curves in the RMSE and PSNR plots indicated improved system performance proportional to the distance

from the center of object space, where best system performance was observed at the center of the array. The MAE and 3D-SSIM plots showed a similar trend, except in the outer two cubic shells (cubic shell 9 and 10). The outer two cubic shells showed improved performance due to enhanced detection at the corners of object space (Fig. 3-4(a)-(d)). The corners of object space represented grid points that were closest to the transducers and hence, were well-detected. Fig. 3-5 shows the results for varying array angular coverage. Similar to the system sensitivity maps in Fig. 3-2, array angular coverage had little to no effect on system performance. Slight variations in system performance in the outer cubic shells of object space are highlighted in the FoM maps (Fig. 3-5(a)-(d)) and quantified in the FoM plots (Fig. 3-5(e)-(h)). The trends in the FoM plots matched the trends from the FoM plots in Fig. 3-4. The MAE and 3D-SSIM plots suggested that the hemispherical array outperformed the other arrays in the outer cubic shells (cubic shells 7-10) of object space. This, however, was likely due to increased detection of only the lower planes of object space. Packing the transducers more tightly allowed for a greater number of transducers to detect voxels closer to the array surface. The results for array radius optimization are given in Fig. 3-6 and indicated improved system performance with decreasing array radius. This was also due to the inverse relationship between system sensitivity and distance (Eq. (8)). At 37.5 mm and 47.5 mm array radius, however, the RMSE and PSNR maps showed voxels in the lower and upper planes of object space that performed poorly. The RMSE and PSNR scores give higher weight to large errors and highlighted regions of poor performance. This trend was also seen in the RMSE and PSNR plots (Fig. 3-6(e) and (f)). System performance was proportional to array radius in the outer cubic shells (cubic shells 7-10) of object space and inversely proportional near the center of object space (cubic shells 6-10). Moreover, the system performance difference between array radii decreased in relation to cubic shell 6. The RMSE and PSNR plots showed cubic shell 6 as the intersection point between the array radius curves and appeared to be independent of array radius. The MAE and 3D-SSIM plots did not reveal anything noticeable at cubic shell 6. As array radius decreased, the FoM curves appeared to flatten, signifying a more uniform system performance throughout object space.

3.4.3 System design strategies and considerations

Most PAT staring, sparse array systems have been designed with transducers arranged into rungs, which appears to be sub-optimal based on the FoM results presented in this work. The uniform sampling arrangement improved system performance over the rung-based arrangement and represents a simple way to enhance future systems. System performance seemed to be independent of array angular coverage in the elevation direction. The MAE and 3D-SSIM measures for the hemispherical array scored better than the other arrays in the outer regions of object space, but, as mentioned above, this was likely due to improved detection for the lower xy-planes in object space.

Nevertheless, increasing the angular coverage of the array also increased the sampling over a larger solid angle and provided for a wider distribution of viewing angles.

Therefore, either more transducers could be mounted on the bowl or the array radius could be reduced. The optimal array radius size would be determined by the dimensions of the desired object space. For the experimental PAT system, the results suggested that the size of object space should be restricted to a cube with dimensions of 1.2 cm x 1.2 cm x 1.2 cm, corresponding to cube contour 5 (Fig. 3- 6(e) and (f)). The FoM indicated that an object space of 2 cm x 2 cm x 2 cm would require a larger array radius (around double the current radius) or that the angular acceptance of the transducers would need to be widened. The size of the array should be increased such that every grid point is detected by each transducer and transducers are positioned as close as possible to object space. A recent approach shown capable of improving imaging performance with a limited number of views was done by treating backscatterers (e.g. steel rods placed behind the object) as virtual transducers [18, 19]. The backscattered acoustic waves contain the backside information (i.e. regions not within view of the array) of an absorbing object and direct these waves to the transducers. Although the work done in [18, 19] utilized raster scanning, the principle could be extended to staring arrays and the spatial crosstalk matrix FoM could be used to optimize the positions of the virtual transducers.

3.5 Conclusion

There has been increased interest in development of imaging systems capable of 3D-PAT with a staring, sparse transducer array. A rational basis for the selection of design parameters that lead to improved transducer array designs will be needed to optimize these new 3D systems. We have examined array designs with respect to angular coverage and FoM derived from the spatial crosstalk matrix (RMSE, PSNR, MAE, and 3D-SSIM) were utilized to assess the effect of transducer arrangement, array angular coverage, and array radius on a truncated spherical transducer array. A uniform sampling arrangement was shown to outperform the rung-based arrangement. Furthermore, we found the FoM to be subtly dependent on the angular coverage of the array, but significantly dependent on the array radius, which implied a trade-off between system performance and field of view.

3.6 Acknowledgments

Philip Wong and Ivan Kosik were supported by the Translational Breast Cancer Research Unit (TBCRU) as well as The University of Western Ontario (WGRS). Philip Wong was also supported by the Ontario Graduate Scholarship (OGS). Avery Raess was supported by WGRS, the Canadian Institute of Health Research (CIHR), and the CIHR strategic training program in Cancer Research and Technology Transfer (CaRTT). Research funding was provided by the Canada Foundation for Innovation (CFI), the Natural Sciences and Engineering Research Council (NSERC), the Canadian Institutes for Health Research (CIHR), the Ontario Ministry of Research and Innovation's Ontario Research Fund (ORF) through the Ontario Preclinical Imaging Consortium (OPIC), and the Lawson Health Research Institute (LHRI). MultiMagnetics Inc. provided matching funds with respect to ORF-OPIC.

3.7 References

1. J. Yao and L. V. Wang, "Photoacoustic tomography: fundamentals, advances and prospects," *Contrast media & molecular imaging* **6**, 332-345 (2011).
2. P. Beard, "Biomedical photoacoustic imaging." *Interface focus* **1**, 602-631 (2011).
3. M. P. Fronheiser, S. A. Ermilov, H. P. Brecht, A. Conjusteau, R. Su, K. Mehta, and A. A. Oraevsky, "Real-time optoacoustic monitoring and three-dimensional mapping of a human arm vasculature," *J. Biomed. Opt.* **15**, 021305 (2010).
4. S. a. Ermilov, T. Khamapirad, A. Conjusteau, M. H. Leonard, R. Lacewell, K. Mehta, T. Miller, and A. a. Oraevsky, "Laser optoacoustic imaging system for detection of breast cancer." *J. Biomed. Opt.* **14**, 024007 (2012).
5. L. Nie, Z. Guo, and L. V. Wang, "Photoacoustic tomography of monkey brain using virtual point ultrasonic transducers," *J. Biomed. Opt.* **16**, 076005 (2011).
6. B. Wang, L. Xiang, M. S. Jiang, J. Yang, Q. Zhang, P. R. Carney, and H. Jiang, "Photoacoustic tomography system for noninvasive real-time three-dimensional imaging of epilepsy." *Biomedical optics express* **3**, 1427-1432 (2012).
7. J. Yao, K. I. Maslov, and L. V. Wang, "In vivo photoacoustic tomography of total blood flow and potential imaging of cancer angiogenesis and hypermetabolism," *Technol. Cancer. Res. Treat.* **11**, 301-307 (2012).
8. I. Y. Petrov, Y. Petrov, D. S. Prough, D. J. Deyo, I. Cicenaitis, and R. O. Esenaliev, "Optoacoustic monitoring of cerebral venous blood oxygenation through extracerebral blood," *Biomedical optics express* **3**, 125 (2012).
9. C. Lutzweiler and D. Razansky, "Optoacoustic imaging and tomography: reconstruction approaches and outstanding challenges in image performance and quantification." *Sensors (Basel, Switzerland)* **13**, 7345-7384 (2013).

10. M. B. Roumeliotis, R. Z. Stodilka, M. a. Anastasio, E. Ng, and J. J. L. Carson, "Singular value decomposition analysis of a photoacoustic imaging system and 3D imaging at 0.7 FPS." *Optics express* **19**, 13405-13417 (2011).
11. A. Buehler, X. L. Deán-Ben, J. Claussen, V. Ntziachristos, and D. Razansky, "Three-dimensional optoacoustic tomography at video rate," *Optics express* **20**, 22712 (2012).
12. X. L. Dean-Ben, A. Ozbek, and D. Razansky, "Volumetric Real-Time Tracking of Peripheral Human Vasculature With GPU-Accelerated Three-Dimensional Optoacoustic Tomography," *IEEE Trans. Med. Imaging* **32**, 2050-2055 (2013).
13. L. Xiang, B. Wang, L. Ji, and H. Jiang, "4-D photoacoustic tomography." *Scientific reports* **3**, 1113 (2013).
14. P. Wong, I. Kosik, and J. Carson, "Objective assessment of 3D photoacoustic tomography by the spatial crosstalk matrix," (under consideration at *J. Biomed. Opt.*).
15. P. Ephrat and J. J. L. Carson, "Measurement of photoacoustic detector sensitivity distribution by robotic source placement," **6856**, 685610-685610--10 (2008).
16. T. Erber and G. M. Hockney, "Equilibrium configurations of N equal charges on a sphere," *Journal of Physics A: Mathematical and General* **24**, L1369 (1991).
17. N. B. Min-Zhi Shao, "Spherical Sampling by Archimedes' Theorem," **MS-CIS-96-02**, (1996).
18. D. Wu, X. Wang, C. Tao, and X. J. Liu, "Limited-view photoacoustic tomography utilizing backscatterers as virtual transducers," *Appl. Phys. Lett.* **99**, 244102-244102-3 (2011).
19. W. Shao-Hua, T. Chao, and L. Xiao-Jun, "Effects of size and arrangement of virtual transducer on photoacoustic tomography," *Chin. Phys. B* **22**, 274-279 (2013).

Chapter 4

4 Discussion and future work

The conclusion to the dissertation is provided in this chapter and insight into future research and development related to the work conducted in Chapters 2 and 3 is discussed.

4.1 Summary of work

Accurate reconstruction of 3D PA images requires detection of photoacoustic signals from many angles. The majority of PAT systems built to date have utilized mechanical scanning of one or more transducers to obtain a sufficient data to reconstruct images. Imaging in the 3D regime by transducer scanning inevitably leads to poorer temporal resolution. Several groups have adopted staring ultrasound arrays, where the transducers are fixed with respect to the imaging cavity, but assessment of array performance has been limited. We previously reported on a method to calibrate a 3D PAT staring array system and analyze system performance using SVD. The SVD metric, however, was computationally expensive and impractical for large system matrices, which are typical for 3D PAT problems.

In Chapter 2, we introduced the crosstalk matrix concept to the field of PAT for system design. The FoM utilized in this study were RMSE, PSNR, MAE, and 3D-SSIM, which were derived between the normalized spatial crosstalk matrix and the identity matrix. The applicability of this approach for 3D PAT was validated by observing the response of the FoM in relation to well-understood PAT sampling characteristics (i.e. PAT system performance improves with increasing spatial and temporal sampling rate). The approach was applied to characterize a 96-element near-spherical staring array PAT system. The results suggested that this formulation could be used to objectively characterize 3D PAT system performance, enabling strategies for system design optimization.

In Chapter 3, we utilized these FoM to characterize and improve a 129-element near-spherical staring array design. Transducer arrangement, array radius, and array angular

coverage were the design parameters examined. We observed that the performance of the 129-element staring transducer array for 3D PAT could be improved by selection of optimal values of the design parameters.

In the following sections, limitations of our work and recommendations for future work are made. Section 4.2 describes several improvements that can be made to the system calibration process. The PA image reconstruction problem was treated as a linear inverse problem, being highly dependent on the calibration of the imaging operator. Therefore, improving the calibration procedure could vastly improve system characterization and imaging performance. Section 4.3 considers the improvement of two other important system design parameters, specifically transducer properties and detection geometry. The limitations of the spatial crosstalk matrix are discussed in section 4.4 as well as the introduction of several other potential system analysis techniques. The primary applications of our real-time 3D PAT system are given in section 4.5.

4.2 System calibration improvements

An important aspect of the calibration procedure that requires improvement is the point source. As discussed in Chapter 2, the current point source did not emit signals uniformly in all directions. Signals traveling upward tended to be weaker than those traveling downward. One possible approach to address this problem is by back-illuminating the point source with the same optical fibers used for imaging. Thus, the light fluence distribution that arises from the placement of the optical fibers would also be accounted for in the imaging operator. Incorporating the light fluence into the forward model has been shown to improve image reconstruction of structures inside tissues [1]. The way the point source is mounted, however, would need to be modified in order to prevent the robot arm from emitting additional PA signals. More complex techniques used to generate an ideal acoustic point source have been studied in the field of acoustic scale model measurements [2] and could potentially be explored for our purposes.

The effects of the shape and size of the point source on system performance are two parameters that would be valuable to study. In particular, the relationship between the dimensions of the point source and the grid resolution (i.e. step size) may provide better insight into the limits of a given system design. The effects of grid point arrangement would be another area to test. For instance, since the back-projected PA signals of the transducers are along spherical shells, calibrating the imaging volume in a spherical coordinate system may improve the mapping of pressure signals to the spatial domain.

Experimentally measuring the imaging operator has the advantage of capturing all the relevant acoustic properties of the system. Imperfections in system design that are difficult to model analytically are accounted for by the calibration procedure, such as slight differences in sensitivity and shape between transducers or blemishes in shell structure. On the other hand, there are difficulties in executing the experimental measurement and the experimental imaging operator also captures system noise. Implementing a simulated imaging operator may enable a more accurate and flexible approach.

4.3 System design considerations

4.3.1 Detector technologies

The work done in Chapter 2 and 3 was only tested for the transducers custom-built in the laboratory. Testing the effect of transducer properties on system performance would be an important step toward identifying improved PAT system performance. Some of the main transducer properties that could be examined are angular acceptance, bandwidth, detector size, detector shape, and piezoelectric material used. All these properties influence the sensitivity and resolution of the transducer, where the ideal transducer would exhibit wide angular acceptance, wide bandwidth, small detector size, and high piezoelectricity. Implementing a combination of different types of transducers could also potentially improve imaging performance. A study done by Geng [3] constructed a wide-band detector by utilizing three transducers, each having a different center frequency

(3.5, 10, and 20 MHz). This approach was shown to improve resolution and contrast in 2D PAT. A recent study utilized two linear arrays with two transducers with different center frequency (6 and 24 MHz) and showed that the multi-bandwidth dataset provided complementary anatomical information for 3D PAT of an excised mouse kidney [4].

There are a wide range of transducer designs, but PA sensors can be generalized into three main categories: piezoelectric, optical, and capacitive micromachined ultrasonic transducers (CMUT). The transducers implemented in this work would be considered piezoelectric sensors. This type of sensor has high sensitivity and is relatively low cost. The aperture size of the piezoelectric sensors, however, is one of the factors that limit the spatial resolution of PAT, where increasing aperture size degrades spatial resolution. Yet, small aperture acoustic detectors are susceptible to thermal noise and are not utilized in practice. Optical sensors and CMUT have better miniaturization qualities than piezoelectric sensors as well as wider bandwidth, but relatively weaker sensitivity [5]. Both optical sensors and CMUT are relatively newer detection technologies and have been successfully applied for PAT [6–10]. These detection technologies hold great potential for improving PAT system performance.

4.3.2 Virtual detectors and reflectors

The concept of the virtual detector was introduced by Li *et al.* for PAM [11,12] and has since been extended to PAT [13–15]. It is one of the approaches taken to overcome the aperture effect by treating a defined focal point of a synthetic aperture or focused transducer as a virtual point detector (Fig. 4-1). Detected signals are delayed by the time corresponding to the focal distance and images are formed either by a delay-and-sum algorithm (for PAM) or back-projection (for PAT). The virtual point detector has high sensitivity compared to that of a real point detector and detects omnidirectionally over a wide acceptance angle. The primary limitation of virtual detector methods is that they require raster scanning of the virtual detector for image reconstruction, compromising temporal resolution. Optimizing system design to incorporate virtual point detectors is another potential area of future work.

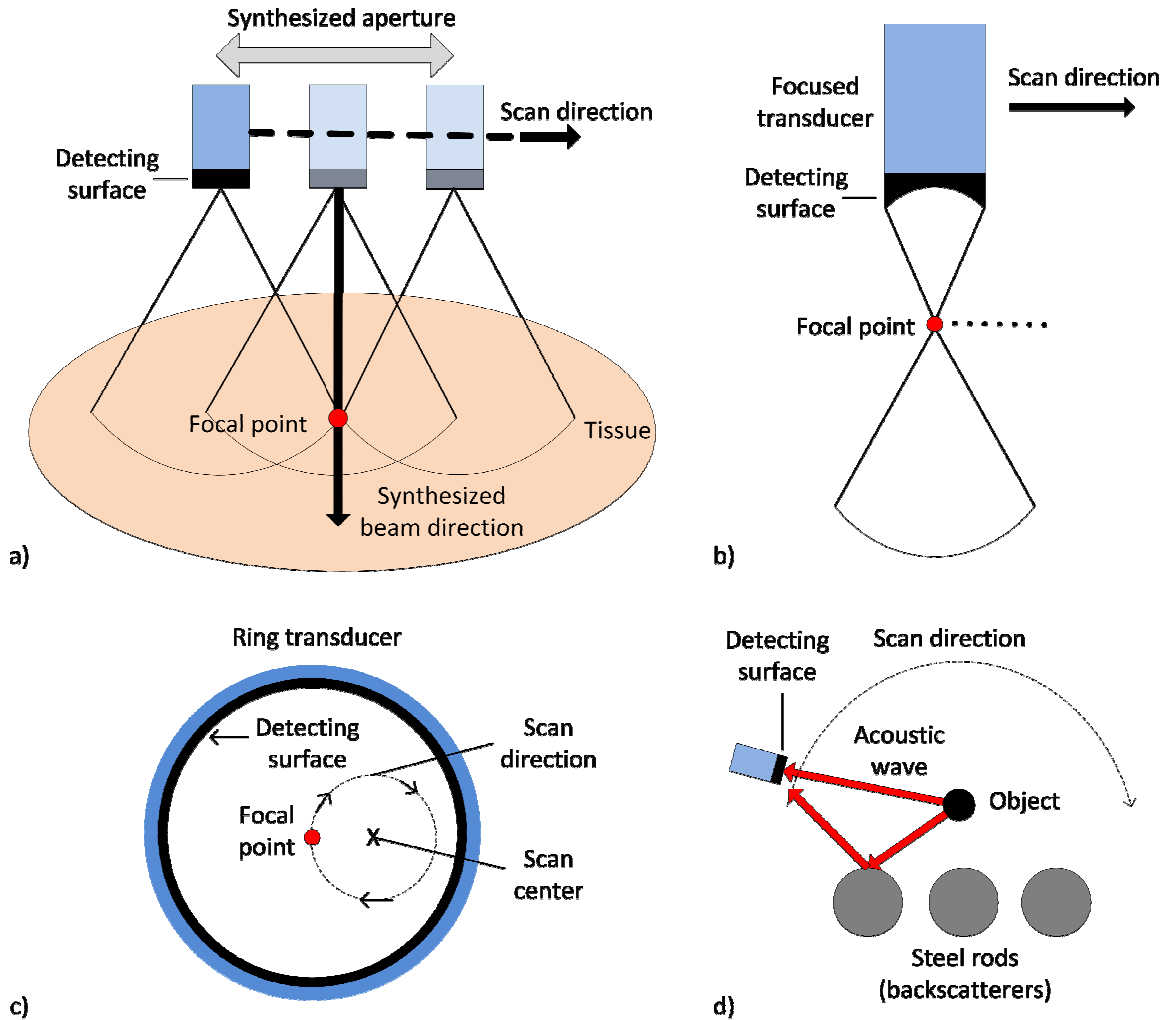


Figure 4-1 Virtual detector concept for a (a) synthetic aperture set up [11,12], (b) focused transducer [13], and (c) ring transducer [14], where the focal point is treated as the virtual detector. The virtual detector is then raster scanned around the object. (d) Illustration of backscatterers as virtual detectors [16]. Acoustic waves containing information of the object at different projections are reflected towards detector.

Another recent approach shown capable of improving limited-view PAT was done by treating backscatterers (e.g. steel rods placed behind an object) as virtual transducers (Fig. 4-1(d)) [16,17]. The virtual transducers are treated as acoustic emitters (or reflectors) that redirect PA waves towards the real transducers. The reflected PA waves contain the backside information of the object (i.e. regions not within view of the array). Although the work done in [16] utilized raster scanning, the principle could simply be extended to staring arrays. Examining different techniques to exploit acoustic reflections holds great potential in transforming the approach taken to PAT system design. For example, constructing the array from acoustically reflective material may improve the

number of projections acquired. More complex geometries could be designed to optimize these acoustic reflections. Acoustic lenses could also be used to focus PA signals onto a detection surface, thereby magnifying a region of the detected object [18].

4.4 System analysis considerations

4.4.1 The crosstalk matrix

The objective assessment of system performance is essential for optimizing the design of PAT systems. As discussed in Chapter 1, Barrett and Gifford first introduced the Fourier crosstalk matrix and applied it to analyze cone-beam tomography [19]. The Fourier crosstalk matrix, however, is not particularly effective for shift-variant imaging systems, due to its inability to spatially localize frequency information. Transducers utilized in PAT have a shift-variant response in object space (non-uniform sensitivity and resolution), making most PAT systems shift-variant. The spatial crosstalk matrix is normally used for shift-variant imaging systems and this work applied the concept for objective assessment of PAT. Nevertheless, similar to the Fourier crosstalk matrix, the spatial crosstalk matrix is not localized in the frequency domain. Transducers also exhibit a frequency-varying response, which is not effectively represented by the spatial crosstalk matrix. Qi and Huesman [20] showed the application of the wavelet crosstalk matrix to assess shift-variant (both spatially- and frequency-varying) imaging systems and demonstrated its advantages. The wavelet crosstalk matrix is based on wavelet series expansions and encapsulates information from both frequency and spatial domains. Deriving figures of merit from the wavelet crosstalk matrix may provide greater insight to system performance than the spatial or Fourier crosstalk matrix alone [20].

4.4.2 Other figures of merit

Since most imaging systems are designed for a general purpose (i.e. with multiple tasks in mind), generic measures are often sought to assess image quality for a given system design. For imaging systems with a specific task, however, system performance can be directly measured using a task-related figure of merit. A recent paper introduced the use

of task-based image quality metrics to compare image reconstruction algorithms in PAT [21]. Task-based metrics help quantify the performance of an observer for a given task. In most clinical applications, the observer seeks to classify different sections in the image. By using a task-based approach, insight into how successful an observer would be in detection or classification for a given task is obtained. For example, one of the main clinical applications for the 3D PAT system presented in this work is breast imaging. When imaging a tumor inside healthy breast tissue, the observer seeks to distinguish (i.e. classify) between healthy tissue and tumor. Task-based assessment is a valuable tool for optimizing PAT system designs for such a classification task.

Furthermore, task-based analysis could be used to optimize the utility of the 3D PAT system for a human observer or for automated assessment. For instance, if the system was sought to be optimized for imaging breast tumor samples in the operating room during breast-conserving surgery (i.e. lumpectomy or partial mastectomy), the ultimate perceiver of the 3D PAT images would be a human observer. If the system was to be used to determine specific traits across a large group of breast cancer patients, then extracting and classifying features could be done using automated techniques. Therefore, depending on the utility of the system, different task-based metrics could be applied to determine system performance.

The focus of the work presented here was to improve real-time, 3D PAT. Since the intended use of the PAT system is for dynamic imaging, system performance could also be assessed according to its ability to track motion. In the same way IQA techniques were applied to the crosstalk matrix in this dissertation, video quality assessment (VQA) techniques could also be applied to the crosstalk matrix. For instance, the 3D-MSSIM could be extended into a 4D-MSSIM metric, where temporal dynamics make up the fourth dimension, by again extending the work which built upon work of others (see Ref. [22]).

4.5 Applications

4.5.1 Functional imaging

One of the major applications of the 3D PAT system developed in this work is 3D functional imaging. The high temporal resolution of the 3D PAT system allows for visualization of dynamic processes when a contrast agent is injected into a small-animal or person. By analyzing voxel-based signal changes produced before, during, and after the administration of a contrast agent, regions within the small-animal can be identified and delineated with respect to their contrast dynamics [23]. Thus, contrast dynamics can provide rich datasets that contain insight into perfusion, pharmacokinetics and physiology.

Aforementioned above, breast imaging is the main clinical application anticipated for the 3D PAT system presented in this work. Dynamic contrast-enhanced (DCE) PAT will potentially enable 3D mapping of blood vasculature in benign and malignant breast tumours. Malignant breast tumours tend to undergo angiogenesis and have ‘leaky’ vessels [24]. Thus, the perfusion dynamics that occur within malignant tumours are distinct from benign tumours and can be used to differentiate between the two groups. Combining DCE methods with 3D PAT carries potential in optimizing the time, cost, and safety of breast cancer examinations.

4.6 Conclusions

The dissertation was intended to introduce the use of objective generic FoM into the field of PAT for optimizing system design. The powerful complement of PAT to existing biomedical imaging technologies was discussed in Chapter 1. The desire to explore objective figures of merit for system performance was driven by the recent transition towards PAT systems with staring arrays, where staring arrays allowed for high temporal resolution 3D imaging. Figures-of-merit based on IQA techniques were derived from the spatial crosstalk matrix in Chapter 2. Upon this foundation, the developed FoM were utilized as a basis for system design parameter optimization strategies in Chapter 3. There

are still many aspects of 3D PAT system design to examine and optimize. Future work could study detector properties (e.g. bandwidth, sensing material, etc.) and detection approaches (e.g. virtual detectors and reflectors).

4.7 References

- [1] S. Bu, Z. Liu, T. Shiina, K. Kondo, M. Yamakawa, K. Fukutani, Y. Someda, and Y. Asao, “Model-based reconstruction integrated with fluence compensation for photoacoustic tomography.,” *IEEE Trans. Biomed. Eng.* **59**(5), 1354–1363 (2012) [doi:10.1109/TBME.2012.2187649].
- [2] J. G. Bolaños, V. Pulkki, P. Karppinen, and E. Hægström, “An optoacoustic point source for acoustic scale model measurements.,” *J. Acoust. Soc. Am.* **133**(4), EL221–7 (2013) [doi:10.1121/1.4793566].
- [3] G. Ku, X. Wang, G. Stoica, and L. V Wang, “Multiple-bandwidth photoacoustic tomography,” *Phys. Med. Biol.* **49**(7), 1329–1338 (2004) [doi:10.1088/0031-9155/49/7/018].
- [4] J. Gateau, A. Chekkoury, and V. Ntziachristos, “Ultra-wideband three-dimensional optoacoustic tomography,” *Opt. Lett.* **38**(22), 4671–4674 (2013).
- [5] C. Lutzweiler and D. Razansky, “Optoacoustic imaging and tomography: reconstruction approaches and outstanding challenges in image performance and quantification.,” *Sensors (Basel)*. **13**(6), 7345–7384 (2013) [doi:10.3390/s130607345].
- [6] E. Zhang, J. Laufer, and P. Beard, “Backward-mode multiwavelength photoacoustic scanner using a planar Fabry-Perot polymer film ultrasound sensor for high-resolution three-dimensional imaging of biological tissues.,” *Appl. Opt.* **47**(4), 561–577 (2008).

- [7] G. Caliano, R. Carotenuto, E. Cianci, V. Foglietti, A. Caronti, A. Iula, and M. Pappalardo, "Design, fabrication and characterization of a capacitive micromachined ultrasonic probe for medical imaging.," *IEEE Trans. Ultrason. Ferroelectr. Freq. Control* **52**(12), 2259–2269 (2005).
- [8] S.-W. Huang, S.-L. Chen, T. Ling, A. Maxwell, M. O'Donnell, L. J. Guo, and S. Ashkenazi, "Low-noise wideband ultrasound detection using polymer microring resonators.," *Appl. Phys. Lett.* **92**(19), 193509–1935093 (2008) [doi:10.1063/1.2929379].
- [9] O. Oralkan and A. Ergun, "Capacitive micromachined ultrasonic transducers: Next-generation arrays for acoustic imaging?," *Ultrason. ...* **49**(11), 1596–1610 (2002).
- [10] G. Paltauf, R. Nuster, M. Haltmeier, and P. Burgholzer, "Photoacoustic tomography using a Mach-Zehnder interferometer as an acoustic line detector.," *Appl. Opt.* **46**(16), 3352–3358 (2007).
- [11] M.-L. Li, H. E. Zhang, K. Maslov, G. Stoica, and L. V Wang, "Improved in vivo photoacoustic microscopy based on a virtual-detector concept.," *Opt. Lett.* **31**(4), 474–476 (2006).
- [12] C. K. Liao, M. L. Li, and P. C. Li, "Optoacoustic imaging with synthetic aperture focusing and coherence weighting.," *Opt. Lett.* **29**(21), 2506–2508 (2004).
- [13] C. Li and L. V Wang, "High-numerical-aperture-based virtual point detectors for photoacoustic tomography.," *Appl. Phys. Lett.* **93**(3), 33902 (2008) [doi:10.1063/1.2963365].
- [14] X. Yang, M.-L. Li, and L. V. Wang, "Ring-based ultrasonic virtual point detector with applications to photoacoustic tomography," *Appl. Phys. Lett.* **90**(25), 251103 (2007) [doi:10.1063/1.2749856].

- [15] L. Nie, Z. Guo, and L. V Wang, “Photoacoustic tomography of monkey brain using virtual point ultrasonic transducers.,” *J. Biomed. Opt.* **16**(7), 076005 (2011) [doi:10.1117/1.3595842].
- [16] D. Wu, X. Wang, C. Tao, and X. J. Liu, “Limited-view photoacoustic tomography utilizing backscatterers as virtual transducers,” *Appl. Phys. Lett.* **99**(24), 244102 (2011) [doi:10.1063/1.3669512].
- [17] S.-H. Wang, C. Tao, and X.-J. Liu, “Effects of size and arrangement of virtual transducer on photoacoustic tomography,” *Chinese Phys. B* **22**(7), 074303 (2013) [doi:10.1088/1674-1056/22/7/074303].
- [18] W. Xia, D. Piras, M. Heijblom, J. C. G. Van Hespén, S. Van Veldhoven, C. Prins, W. Steenbergen, T. G. Van Leeuwen, and S. Manohar, “Enlarged acceptance angle of a finite size detector in photoacoustic imaging using acoustic lenses,” 9 June 2011, 80900L–80900L–7 [doi:10.1117/12.889970].
- [19] H. H. Barrett and H. Gifford, “Cone-beam tomography with discrete data sets.,” *Phys. Med. Biol.* **39**(3), 451–476 (1994).
- [20] J. Qi, S. Member, and R. H. Huesman, “Wavelet Crosstalk Matrix and Its Application to Assessment of Shift-Variant Imaging Systems,” 123–129 (2004).
- [21] A. Petschke and P. J. La Rivière, “Comparison of photoacoustic image reconstruction algorithms using the channelized Hotelling observer.,” *J. Biomed. Opt.* **18**(2), 26009 (2013) [doi:10.1117/1.JBO.18.2.026009].
- [22] I. I. Conference and I. Processing, “3D-SSIM FOR VIDEO QUALITY ASSESSMENT Kai Zeng and Zhou Wang,” 1–4 (2012).
- [23] E. M. C. Hillman, C. B. Amoozegar, T. Wang, A. F. H. McCaslin, M. B. Bouchard, J. Mansfield, and R. M. Levenson, “In vivo optical imaging and dynamic contrast methods for biomedical research.,” *Philos. Trans. A. Math. Phys. Eng. Sci.* **369**(1955), 4620–4643 (2011) [doi:10.1098/rsta.2011.0264].

- [24] L. W. Turnbull, “Dynamic contrast-enhanced MRI in the diagnosis and management of breast cancer.,” *NMR Biomed.* **22**(1), 28–39 (2009) [doi:10.1002/nbm.1273].

Curriculum Vitae

Name: Philip Wong

Post-secondary Education and Degrees: The University of Western Ontario
London, Ontario, Canada
2012-2014 M.Sc.

The University of Western Ontario
London, Ontario, Canada
2008-2012 B.M.Sc.

Honours and Awards: Province of Ontario Graduate Scholarship (\$15,000)
2013-2014

Translational Breast Cancer Research Unit Research Studentship
2012-2014 (\$34,000)

Western Graduate Research Scholarship (\$9,000)
2012-2014

Dean's Honour List
2010-2012

Western Scholarship of Excellence
2008

Related Work Experience Research Assistant
The University of Western Ontario
2011-2014

Publications:

Submitted or Under Revision

Wong, P, Kosik, I, and Carson, J.J.L. Objective assessment of 3D photoacoustic tomography by the spatial crosstalk matrix. *Journal of Biomedical Optics*, In Preparation.

Wong, P, Raess, A, Kosik, I, and Carson, J.J.L. Design improvement of a staring, sparse transducer array for 3D photoacoustic tomography using the spatial crosstalk matrix. *Journal of Biomedical Optics*, In Preparation.

Manuscripts in preparation

Wong, P, Kosik, I, and Carson, J.J.L. Virtual detector array for photoacoustic tomography.

Conference Presentations, Abstracts, and Proceedings

Wong, P, Kosik, I, and Carson JLL. Imaging operator optimization for a 3D photoacoustic system and rolling singular value decomposition analysis. Podium presentation at 2013 Artimino Ultrasound Conference, Lake Rosseau, ON.

Wong, P, Vasefi, F, Brackstone, M, and Carson JLL. Hyper-spectral imaging of tissue mimicking phantoms: principle component analysis. Podium presentation at 2013 SPIE BiOS Photonics West Conference, *Optical Interactions with Tissue and Cells XXIV*, San Francisco, CA.

Wong, P, Kosik, I, and Carson JLL. Dynamic contrast-enhanced 3D photoacoustic imaging. Poster presentation at 2013 SPIE BiOS Photonics West Conference, *Photons Plus Ultrasound: Imaging and Sensing*, San Francisco, CA.

Wong, P, Kosik, I, and Carson JLL. Dynamic contrast-enhanced 3D photoacoustic imaging. Poster presentation at 2013 London Health Research Day, London, ON.

Wong, P, Kosik, I, and Carson JLL. Dynamic contrast-enhanced 3D photoacoustic imaging. Poster presentation at 2013 Oncology and Research Education Day, London, ON.

Wong, P, Vasefi, F, Brackstone, M, and Carson JLL. Hyper-spectral imaging of tissue mimicking phantoms: principle component analysis. Poster presentation at 2012 London Health Research Day.